Ludwig-Maximilians-Universität München

Development of a milli-Kelvin THz Setup for Photovoltage Experiments on 2D Materials

Entwicklung eines Milli-Kelvin-THz-Aufbaus für Photospannungsexperimente an 2D-Materialien

Master Thesis

von

Leon Gabriel Schubert

Chair of Experimental Solid State Physics
Quantum Materials

Supervisors:
Prof. Dr. Dmitri K. Efetov
Giorgio Di Battista

16.09.2024

Contents

Abstract

Electromagnetic radiation is one of the drivers of modern scientific progress, where understanding and control of new frequency ranges have repeatedly led to a multitude of groundbreaking advancements. One of the most underdeveloped frequency ranges is hereby the Terahertz (THz) region caused by the difficult accessibility via traditional means. In this work, we establish the foundation for a THz photovoltage setup at milli-Kelvin temperatures for experiments on two dimensional Magic-angle twisted bilayer graphene and its unconventional superconductivity. It is based on a GaAs Photomixer located at the still plate (1K) stage of a dilution refrigerator. This setup aims to provide insights into intra-band transitions of correlated electrons and achieve single-photon sensitive detection at THz frequencies.

Chapter 1

Introduction

The Terahertz spectral range is located in-between the microwave and infrared spectrum around f_{THz} ~1 THz and λ ~300 μm. Historically, this part of the electromagnetic spectrum has been severely underdeveloped, also known as the "THz Gap".

The energy of THz photons ~meV is too low for traditional optoelectronics based on semiconductor interbandtransitions. At the same time, its frequency >300 GHz is too high for radio and microwave electronics. To bridge this gap, many novel emitters like free electron and quantum cascade lasers, backward wave oscillators and photomixers have been developed over therecent years [38]. They give us access to study a large range of physical, biological and chemical phenomena (including superconductivity) that depend on meV transitions [53]. Additionally, a large number of potential detector configurations and materials have been investigated and two-dimensional (2D) materials like magic angle twisted bilayer graphene (MATBG) are promising candidates that can theoretically reach the single photon limit [41].

The field of 2D materials has recently developed into a central branch of modern solid state physics with a wide variety of novel phenomena and technological applications [43]. The field remained somewhat niche up until the breakthrough of Novoselov and Geim in 2004 [35], which revolutionised the research on 2D materials. Their method of repeatedly exfoliating bulk graphite crystal on a scotch tape is not only extremely simple but also produced single layer graphene (SLG) of previously unprecedented quality and size. It can also be employed to create a large variety of other atomically thin materials from van-der-Waals materials with weak inter-layer binding. They include other single-element crystals, compounds, salts and polymers. For the purpose of this thesis, graphene and hexagonal boron nitride (h-BN) are of particular interest.

Soon thereafter it was discovered that stacking two SLG sheets and inducing a relative twist has a profound impact on the electronic band structure by creating a long range order [30] [11]. The "magic-angle" of θ=1.1° hereby presents a special case with the formation of flat bands, which possess a large number of correlated electron states. Its 2D nature hereby provides an *in situ* method for precise tunabilty of the electronic filling factor via an external gate [11]. It is therefore a highly promising material which can provide insight into correlated insulators, strange metal phases, heavy fermions as well as unconventional superconductivity (SC).

Chapter 2

Theoretical Background

In this chapter we discuss the basic theoretical backround of opto-electronic processes within 2D heterostructures. We begin by analyzing the bandstructure in SLG and then extend this framework to bilayer and magic-angle graphene with the goal of describing the highly correlated states within MATBG.

2.1 Band Structure of Graphene

In the unbound ground state, the 6 electrons surrounding the carbon nucleus are located in the $1s^2 2s^2 2p^2$ orbitals with opposing spins in doubly occupied states [44].

When an atom enters a molecular bond, it can be energetically favourable for one of the 2s electrons to move up into the 2p shell and form new hybridised states with the original 2p states. The resulting linear combination of the 2s and 2p orbitals can form σ-bonds with surrounding atoms which are usually only accessible to s-electrons. The σ-bonds are bound much stronger than the outer π-bonds of unhybridized 2p states [16]. The energy gain from the bond creation exceeds the energy cost required to hybridise s and p electrons. Three hybridisation configurations are possible, namely sp, sp^2, sp^3 depeding on the number of p-electrons involved. In graphene the carbon atoms each possesses three electrons in the sp^2 state which bond in a planar configuration to three neighbouring atoms as well as a single p electron that

(a) **(b)**

Figure 2.1: Electron configuration in carbon a) Unbound ground state of carbon. b) Depiction of the hybridised sp^2 bonds in graphene with the remaining p electrons located out of plane. Image adapted from [3].

is located outside of the plane and only engages in weak π-bonds. The individual σ-bonds repel each other and settle at an equidistant angular spacing of 120°, which gives rise to the familiar honeycomb lattice when extended in plane. It can be described by two triangular lattices, dividing the atoms in two sets A and B with lattice vectors:

$$\vec{a}_1 = \frac{a}{2}(3, \sqrt{3}) \qquad \vec{a}_2 = \frac{a}{2}(3, -\sqrt{3}) \tag{2.1}$$

The lattice constant which determines the distance between atoms in the unit cells is hereby given as $a \approx 2.46$ Å. We can also calculate the reciprocal lattice vectors b_i from their relation,

$$\vec{a}_i \cdot \vec{b}_j = 2\pi\delta_{ij} \tag{2.2}$$

giving,

$$\vec{b}_1 = \frac{2\pi}{3a}(1, \frac{1}{\sqrt{3}}) \qquad \vec{b}_2 = \frac{2\pi}{3a}(1, -\frac{1}{\sqrt{3}}) \tag{2.3}$$

With the reciprocal vectors b_i we can now construct the first Brillouin zone of graphene as depicted in Figure 2.2b. The corner points K and K', also called Dirac points, are hereby of particular importance and located at the reciprocal coordiantes:

$$\mathbf{K} = (\frac{2\pi}{3a}, \frac{2\pi}{3\sqrt{3}a}) \quad \mathbf{K'} = (\frac{2\pi}{3a}, -\frac{2\pi}{3\sqrt{3}a}) \tag{2.4}$$

The electronic band structure is mainly defined by the loosely bound 2p-electrons as they are able to move in-between different lattice sites via the π-bonds. If we only consider nearest neighbour hopping, the process can be described by the tight-binding Hamiltonian,

$$\hat{H} = -t \sum_{\langle i,j \rangle, \sigma} (a^\dagger_{\sigma,i} b_{\sigma,j} + H.c.) \tag{2.5}$$

Hereby $a^\dagger_i, b^\dagger_i, a_i, b_i$ designate the creation and annihilation operators of neighbouring sites $\mathbf{R}_i$ and $\mathbf{R}_j$ on the sub-lattices A and B. t describes the energy required for nearest neighbour hopping ($t \approx 2.8$), while the spin of individual electrons is denoted via $\sigma = \uparrow, \downarrow$ and units are set such that $\hbar = 1$ [13].

By Fourier transforming the operators, we can translate the Hamiltonian into the reciprocal space:

$$a^\dagger_i = \frac{1}{\sqrt{N}} \sum_k e^{ikr_{i,A}} a^\dagger_k \qquad b^\dagger_j = \frac{1}{\sqrt{N}} \sum_k e^{ikr_{j,B}} b^\dagger_k \tag{2.6}$$

$$\hat{H}(k) = -t \sum_{k,j} (e^{ik\cdot\delta_j} a^\dagger_k b_k + H.c.) \tag{2.7}$$

The vector δ_j hereby describes the real-space vectors of nearest neighbours and therefore hopping paths:

$$\sigma_1 = \frac{a}{2}(1, \sqrt{3}) \qquad \sigma_2 = \frac{a}{2}(1, -\sqrt{3}) \qquad \sigma_3 = a(1, 0) \tag{2.8}$$

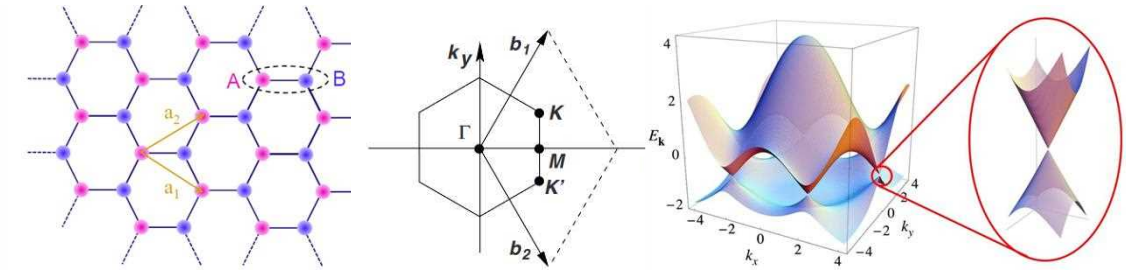

(a) (b) (c)

Figure 2.2: Graphene lattice and band structure a) Subdivision into two triangular sublattices A (pink) and B (blue) [15]. b) Reciprocal lattice vectors with corresponding Brillouin zone [13]. c) Band structure of the honeycomb lattice with enlarged view of one Dirac point at K/K' [13]

.

After this transformation, the Hamiltonian is in a block-diagonal shape and we can calculate the eigenvalues to [13]:

$$E_{\pm}(\mathbf{k}) = \pm t\sqrt{3 + f(\mathbf{k})} \quad f(\mathbf{k}) = 2cos(\sqrt{3}k_y a) + 4cos(\frac{\sqrt{3}}{2}k_y a)cos(\frac{3}{2}k_x a) \tag{2.9}$$

The resulting dispersion relation is shown in Fig. 2.2c, with a magnified view of one of the Dirac points. At this location ($\mathbf{K}$ / $\mathbf{K'}$) in the Brillouin zone the upper and lower bands touch forming a semi-metal.

We can calculate the dispersion relation at these points by introducing a small momentum perturbation $\mathbf{q}$ such that $\mathbf{k} = \mathbf{K} + \mathbf{q}$ and recieve a massless Dirac Hamiltonian:

$$h(\mathbf{K} + \mathbf{q}) = \hbar\nu_F \begin{pmatrix} 0 & q_x + iq_y \\ q_x - iq_y & 0 \end{pmatrix} = \hbar\nu_F \mathbf{q} \cdot \sigma \tag{2.10}$$

with an effective Fermi velocity of $\nu_F = -t\frac{3a}{2}$ and a liner dispersion relation:

$$E_{\pm}(\mathbf{q}) = \pm\hbar\nu_F|\mathbf{q}| \tag{2.11}$$

During these calculations, the additional higher order terms like next nearest-neighbour hopping are neglected. Their contribution creates a small asymmetry between the valance (π) and conduction ($\pi*$) bands. However, it can be demonstrated that the combination of C_2 and T (spatial and time-inversion) symmetry prevent the opening of a gap at the Dirac points and preserves the semimetalic nature of graphene around the $\mathbf{K}$ points [15]. As soon as this C_2T symmetry is broken, a band gap will develop which is crucial for understanding the band structure of MATBG.

2.2 Bilayer Graphene

The initial tight binding model of graphene can be extended by additional interlayer hopping parameters to cover bi- and mulit-layer graphene. The ground state crystal

arrangement of stacked graphene and in bulk graphite is the AB configuration in Figure 2.3a. After taking the three additional nearest-neighbour hopping paths into account while ignoring spin, the resulting Hamiltonian amounts to [13],

$$\begin{aligned}\hat{H} = &-\gamma_0 \sum_{\langle i,j\rangle,m} (a^\dagger_{m,i} b_{m,j} + H.c.) \\ &- \gamma_1 \sum_j (a^\dagger_{1,j} a_{2,j} + H.c.) \\ &- \gamma_2 \sum_j (a^\dagger_{1,j} b_{2,j} + a^\dagger_{2,j} b_{1,j} + H.c.) \\ &- \gamma_3 \sum_j (b^\dagger_{1,i} b_{2,j} + H.c.)\end{aligned} \tag{2.12}$$

with the first component being the original intra-layer Hamiltonian ($\gamma_0 = t$) and m=1,2 denoting the layers. In the continuum limit the eigenvalues can be calculated to

$$E^2_\pm(\mathbf{k}) = V^2 + \nu_F^2\mathbf{k}^2 + t_\perp^2/2 \pm \sqrt{4V^2\nu_F^2\mathbf{k}^2 + t^2\nu_F^2\mathbf{k}^2 + t_\perp^4/4} \tag{2.13}$$

V hereby symbolises an external electric potential, orientated perpendicular to the planes and the inter-layer hopping parameters $\gamma_1, \gamma_2, \gamma_3$ are combined into an effective inter-layer hopping energy $t_\perp$ ($\approx$ 0.4 eV) ¡ t ($\approx$ 2.5 eV) [15]. Taking the assumption of small momenta $\mathbf{q}$ and $V \ll t$ we can approximate the dispersion relation to:

$$E \pm (\mathbf{k}) \approx V - 2V\nu_F^2\mathbf{k}^2/t_\perp + \nu_F^4\mathbf{k}^4/2t_\perp^2 V \tag{2.14}$$

In the equilibrium state with no potential shift between the two graphene layers ($V = 0$), the crystal remains a gap-less semimetal. However, as soon as an external field is allied ($V \neq 0$), the inversion symmetry C_2 between the layers is broken due to their relative potential offset. The Dirac point is no longer symmetry-protected and a subsequent band gap emerges.

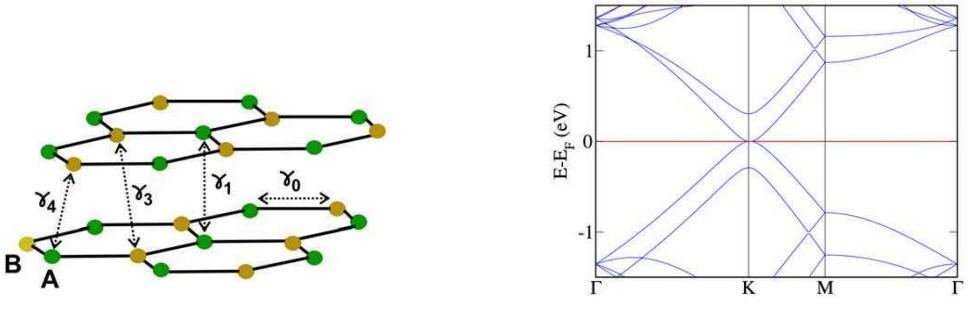

(a) **(b)**

Figure 2.3: Configuration of AB-graphene a) Lattice structure with nearest-neighbour hopping paths. Figure from [13]. b) Resulting bandstructure in ground state AB-bilayer. Graph from [1]

2.3 Twisted Bilayer Graphene

When overlaying two identical periodic geometric lattices and inducing some relative twist angle, a new larger scale (Moiré) pattern emerges. We can translate this concept to 2D solid state materials which creates a complex crystal structure with long range order called superlattice which inherits interesting emergent properties. The lattice vectors L_1 and L_2 of this new twisted bilayer graphene (TBG) material are given by,

$$L_1 = ma_1^{(1)} + na_2^{(1)} = m'a_1^{(2)} + n'a_2^{(2)} \tag{2.15}$$

L_2 is hereby calculated by rotating L_1 by 60° From these two vectors, we devise the superlattice constant L as well as the size of a unit cell S:

$$L = a\sqrt{m^2 + n^2 + mn} = \frac{|m-n|}{2sin(\theta/2)}a \tag{2.16}$$

$$S = |L_1 \times L_2| = (\sqrt{3}/2)L^2 \tag{2.17}$$

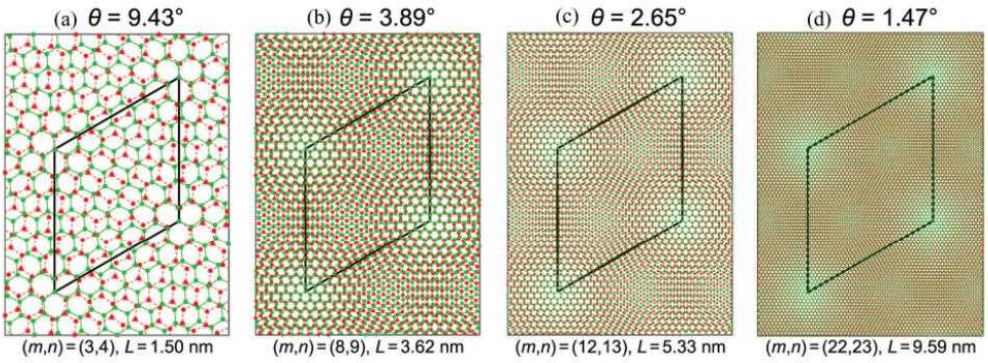

Figure 2.4: Moiré pattern in graphene. Commensurate angles that lead to superlattices of different sizes [34].

The resulting crystal structure of TBG is generally aperiodic except at specific twist angles, where the moiré pattern repeats at certain intervals. Those so called commensurate configurations can be classified via two positive coprime integers m and n [34]:

$$cos\theta(m,r) = \frac{1}{2}\frac{m^2 + n^2 + 4mn}{m^2 + n^2 + mn} \tag{2.18}$$

For our purposes, the main interest lies with the small angle limit which contains the most fundamental lattices $|m-n| = 1$ that only possess one moiré pattern per unit cell.

We can then utilise this knowledge of the superlattice geometry to construct the significantly smaller moiré Brillouin zone (Figure 2.5) as well as find an expression of the superlattice carrier density n_S.

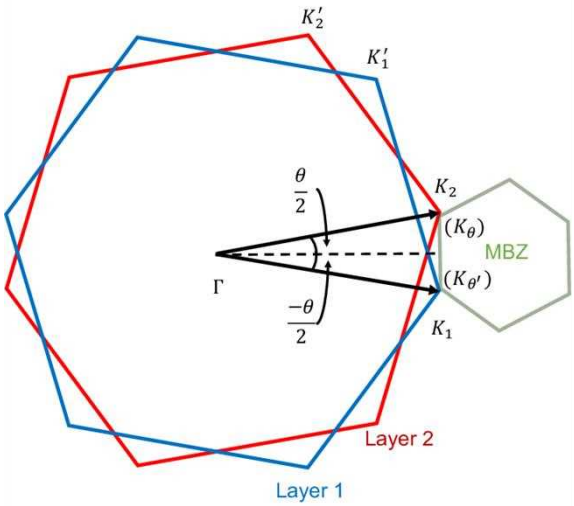

Figure 2.5: Moiré Brillouin zone Two rotated Brillouin zones that fold into a mini moiré zone. Image taken from from [25]

$$n_S = 4\frac{8sin^2(\theta/2)}{a^2\sqrt{3}} \approx \frac{8}{a^2\sqrt{3}}\theta^2 \quad \text{for} \quad |m-n| = 1 \quad \text{and small} \quad \theta \tag{2.19}$$

Hereby we take both the spin (σ) and valley (K and K') degeneracy into account leading to a prefactor of 4. The resulting relation will become very useful in Chapter 6 as we can calculate the local twist angle in our material from the point where the charge carrier density n reaches the complete moiré filling [48].

$$n = \frac{V_g - V_{g0}}{e}\frac{d_{hbn}}{\epsilon_0\epsilon_{hbn}} \tag{2.20}$$

Where $V_g - V_{g0}$ is the gate offset from the charge neutrality point, d_{hbn} and ϵ_{hbn} are the h-BN gate thickness and dielectric constants. H-BN is hereby an ideal gate dielectric as it prevents gate shorting as well as distortion of the TBG band structure owing to its large bandgap [11]

As depicted in Figure 2.4, the size of the moiré cell as well as the number of atoms contained within rises significantly when we go to lower angles. Analysing the electronic structure within this range via the tight binding model becomes quite extensive, as we need to consider all possible hopping paths within the superlattice cell [39]. If we stay close to the low-energy and low-momentum limit, we can utilise the much simpler continuum model [29] [40]. Instead of deriving the Hamiltonian from all potential inter-layer hopping interactions and then diagonalising the large non-trivial matrix, the continuum model starts off with two independent single-layer wavefunctions that hybridise via their mutual interactions [15]. The Hamiltonian of this system consists of the two SLG components H_1 and H_2 with an additional inter-layer interaction term $H_\perp$. As we are mainly interested in the phenomenological consequences of this hybridisation process, we will not be discussing the extensive calculations of this model which can be found in [29] [30].

The results imply a strong dependence of the hybridisation term on θ as well as twist induced particle-hole symmetry breaking at small angles [30].

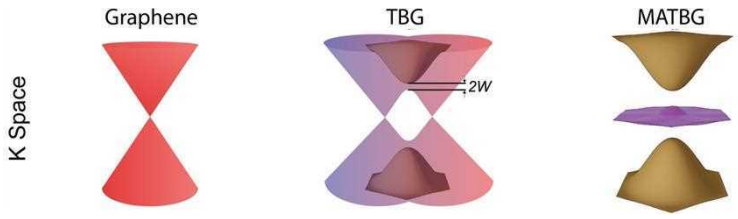

Figure 2.6: Hybridisation of the Dirac cones forming flatbands. Figure addapted from [6] showing the unhybridised SLG, large twist angle interactions and magic-angle flattbands.

2.4 MATBG Flatbands

Remarkably, describing the resulting moiré bands only requires a single parameter α that is dependent on the ratio between the inter-layer coupling ω and kinetic energy $v_F k_\theta$ [7]:

$$\alpha = \frac{\omega}{\hbar v_F k_\theta} \tag{2.21}$$

At angles of $> 5^\circ$ the K points of the two layers are spaced far away from each other and their Dirac cones are lightly coupled ($\alpha \ll 1$), which only leads to a small mutual distortion [6]. At lower values of θ, the increasing overlap induces stronger interaction and thus more hybridisation. Therefore the Fermi velocity also renormalises to a new value of [7]:

$$v_F^* = v_F \frac{1 - 3\alpha^2}{1 + 6\alpha^2} \tag{2.22}$$

A striking consequence hereby is that for $\alpha = \sqrt{3}^{-1}$ the renormalized Fermi velocity approaches 0. This corresponds to a "magic" twist angle of $\theta = 1.1^\circ$, where the Dirac cones merge to form an ultra flat electronic band in the center surrounded by two band gaps (Figure 2.6). This resulting flatband only possesses a bandwidth of 10 meV and therefore a very high density of states and electron correlation [6].

When the Fermi level is located within this central band, the electron-electron Coulomb interactions increase far beyond their kinetic energy which leads to the emergence of strongly correlated states which give rise to several interesting phenomena including correlated insulators, strange metal phases and most interestingly superconductivity [11].

2.5 Thin Film Superconductivity

Below a critical temperature T_C, electrons with spin (S=1/2) can overcome mutual coulomb repelling to form spin-less (S=0) cooper pairs. They do not scatter, possess no resistance and form a perfect diamagnet as any magnetic field will induce a permanent opposing current [33]. Similarly to the critical temperature, the SC also possesses a critical current and therefore field at which the cooper-pair is broken. The description for conventional superconductors (BCS) was fully established by Bardeen, Cooper and Schrieffer in 1957 [4]. In this description, the necessary coupling arises from a virtual exchange of phonons. It became apparent that there is another class of SC that is not covered by the previous theory, unconventional superconductivity. It does not require lattice vibration but instead relies on strongly correlated electron physics. To this date, 9 different classes of superconductivity and over 200 different SC cuprates have been found [45] some with remarkably high transition temperatures. However, the origin of unconventional superconductivity is not fully understood to this day.
MATBG is hereby an interesting unconventional 2D superconductor with some resemblance to cuprates [12]. The critical temperature (T_C = 1.7K) and superconducting gap ($\approx$1 meV) are surprisingly high, indicating very high coupling strength that has to compensate for the extremely small Fermi surface of MATBG [12]. With the small number of electrons per atom as well as its exceptional thinness, MATBG possesses an extremely low charge carriers count per unit area $\sim 10^{11}$ cm^{-2} that is unmatched by any other SC material. These properties make MATBG highly interesting for studying correlated systems, novel devices and high T_C superconductors.

Chapter 3

Fabrication

This chapter will explore the fabrication and assembly of 2D hallbar devices, highlighting the creation of gated heterostructures from bulk graphene and hexagonal boron nitride (h-BN) crystals. An in-depth description of our methodology can be found it the recent publication [18].

3.1 Exfoliation & Flake Search

Over recent years, a large number of fabrication methods for obtaining mono-layer atomic materials have been developed [20]:

- Mechanical, ultrasonic and electrochemical exfoliation
- Plasma etching
- Chemical vapor deposition
- Van der Waals and molecular beam epitaxy
- Solvothermal method

To this day, mechanical exfoliation via a simple scotch tape still remains the most common method. It is possible due to the weak inter-layer Van der Waals binding and offers the best crystal quality, ease of use as well as short fabrication time. We hereby follow the technique refined by Hunag et al. [22] and begin by preparing small ($\sim$ 5mm $\times$ 5mm) square silicon substrates with a 285 nm oxide layer cut from a larger waver. They are then cleaned with O_2 Plasma for higher surface roughness to increase adhesion during exfoliation. The bulk van-der-Waals crystal is then repeatedly placed and lifted off on a small section of a scotch tape until it is densely covered. We then perform repeated exfoliations until the entire length of the tape is covered. For the case of h-BN we make use of a second "daughter" scotch tape. It is paced on the initial tape after exfoliation and it has increased crystal density around the desired thickness $\sim$5-20 nm. In the next step, the exfoliated strip is then pressed on the silicon chip for approximately one minute, with significant force for graphite and only lightly for the more fragile h-BN. After heating to $\sim$ 105°C for

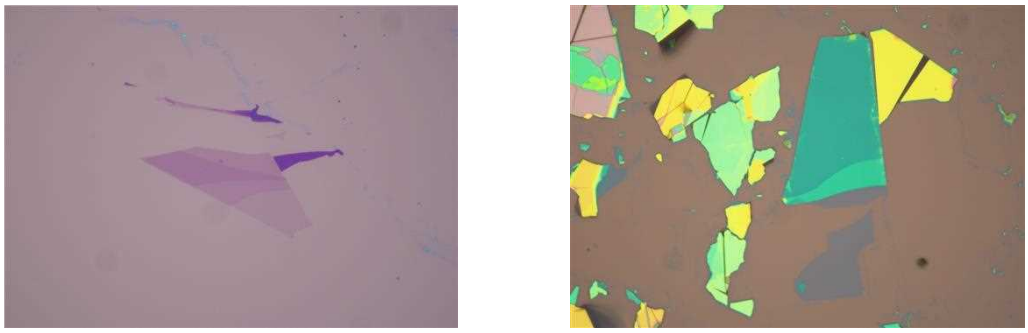

(a) **(b)**

Figure 3.1: Colour shift from graphene and h-BN flakes on silicon wavers a) Central graphene flake with single, bi and tri layer sections as well as a much thicker region (>5 layers) b) h-BN flakes of widely different heights, dark blue in bottom center <10nm, turquoise 10-20nm, yellow & green significantly thicker and thus not suitable for stacking.

$\sim$ 2 min (which is not done for the h-BN to avoid glue residue), the tape is slowly peeled leaving a large number of crystal fragments of different size and thickness on the waver.

Before the stacking and fabrication can begin, we need to first select viable flakes of the right thickness and quality. The silicon oxide layer on the substrate plays a pivotal role as it induces Bragg reflection $n\lambda = 2\ d\ sin(\theta)$ due to the second material interface between oxidised and pure silicon. Any crystal on the chip surface modifies the interface distance d and therefore the wavelength of reflected light. This allows us to observe thin film materials and their thickness even though they would be virtually invisible under other circumstances, with single layer graphene absorbing only $\approx$2.3% of optical light [31]. Figure 3.1 depicts the colour variations under an optical microscope between different layer heights.

This lets us search for flakes of the right thickness, size and quality and the requirements for one standard MATBG-hallbar device are:

- Two hHN-flakes with heights of 5-20nm to encapsulate the device and form a dielectric barrier between gate and the graphene layers. Thinner flakes generally yield better devices with increased homogeneity due to their higher flexibility. Additionally, they increase the visibility of unwanted aberrations like bubbles, cracks and contaminations. On the other hand, thinner flakes tend to be more fragile and can tear more easily while assembling a stack. An additional criterion is size, which needs to be larger than the subsequent graphene and graphite crystals to ensure full encapsulation as well as prevent gate leaks. One of the flakes should also possess a straight edge for graphene clamping during the stacking process.

- A single layer graphene flake of sufficient size >15µm × 30µm, at least twice of the final device. It should be as pristine as possible without any thicker regions or potential points of failure.

- A rectangular $\sim$ 5-10 layer, $\sim$2-4 nm thick graphite flake which forms the basis of our bottom gate. Its length should be slightly larger than the shorter side of

our graphene flake for better access during electronic contacting. An optimal width lies in-between 3µm and 8µm to ensure a sufficient device size as well as sideways protruding graphene for the future hallbar arms.

During this process we also pay attention to the area surrounding a potential flake. Thick material in the vicinity can prove detrimental to a smooth and successful pick-up process and are to be avoided if possible. Examples for high quality flakes suitable for stacking are depicted in Figure 3.2

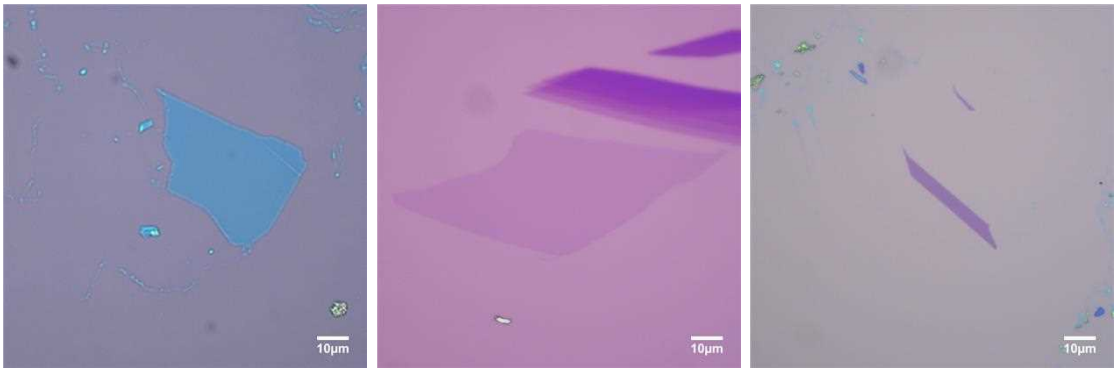

(a) **(b)** **(c)**

Figure 3.2: Selected flakes for stacking a) H-BN with clamping edge on the top right. b) Large single layer graphene crystal. c) Graphite flake for gating.

3.2 Stacking

In order to move, manipulate and assemble 2D-material flakes, a raised polymer layer on one end of a microscope slide is used. These so-called stamps were initially made from Polydimethylsiloxane (PDMS) exclusively. Later developments lead to the use of thin films of Polypropylene-carbonate (PPC) and recently Polycarbonate (PC). This provides several advantages which include superior adhesive properties and an inherent glass–liquid transition at around $T_G \approx 145°C$ [42] making the viscosity and adhesion much more controllable at higher temperatures. PDMS is also still in use as a support and cushioning platform for the PC film. The stamp assembly process itself is quite crucial as the final stamp quality can significantly impact the stacking experience. Therefore we will further elaborate on this method, beginning with the creation of a thin layer of PC.

3.2.1 Creation of PC Film

- We dissolve PC granulate from Sigma Aldrich in Chloroform to create a 6% solution by weight and then stir it for several hours, preferably over night.

- New glass slides are rinsed with Acetone and propan-2-ol (IPA) to maximise their cleanliness and then blow dried with compressed nitrogen.

- When all of the remaining IPA has evaporated, we spread approximately 10 drops of our PC solution in a wavy motion along the long center axis of the slide.
- A second cleaned glass substrate is dropped on top as quickly as possible to minimize initial Chloroform evaporation. The top slide is then gently pulled off sideways with the goal of distributing the polymer as homogeneously as possible.
- Afterwards we dry both slides on a 100° C hot plate for 3 minutes to evaporate the Chloroform solvent.

3.2.2 Stamp Assembly

As soon as our PC-films have fully solidified and cooled down, we can begin the process to stamp assembly.

- We use a scalpel to cut a small square ∼3mm ×3mm from a PDMS sheet made by Gel-Pak. It has a 0.5 mm thickness and is enclosed by two protective polymer sheets.
- Afterwards, we remove the protective layers and place it in an Ossila UV Ozone cleaner for 15 min. This leads to better adhesion in-between the polymers and therefore higher stamp quality down the line.
- A strip of scotch-tape is placed on a clean surface and a square of ∼5mm ×5mm is cut into it with the same precision knife.
- With the resulting window, we then pick up a clean & homogeneous area of previously prepared PC and place it on top of the PDMS square at the end of a new glass slide.
- During this process the PC should stay as immaculate as possible and wrinkles in the polymer are to be avoided.
- After gluing the polymer layers in position with additional tapes, the finished stamp is heated to 110°C for 5 minutes which increases PC-PDMS adhesion.

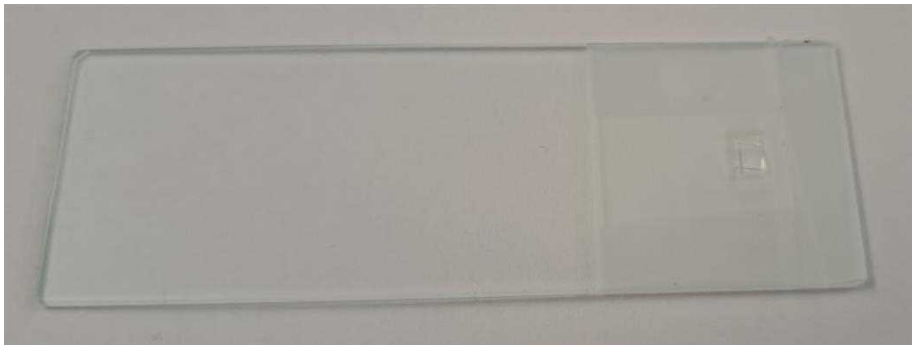

Figure 3.3: Typical PC-PDMS stamp used for stacking

3.2.3 Stacking

The stacking process is done in a semi-manual transfer stage, which consist of an upper and lower stage (Fig. 3.4). They are designed to hold the stamp and silicon substrate respectively and proper attachment is ensured via a vacuum system. The upper assembly is mounted on a translation stage that allows for precise 3 axis positioning as well as two axis tilt adjustment via 5 high precision set-screws. The lower stage is anchored to a servo motor driven and electronically controlled horizontal translation stage. It also houses precise rotation stage and a heater for temperature control during the stacking process. An optical microscope with large focal length and a magnification of up to $\times 100$ is located directly above the assembly.

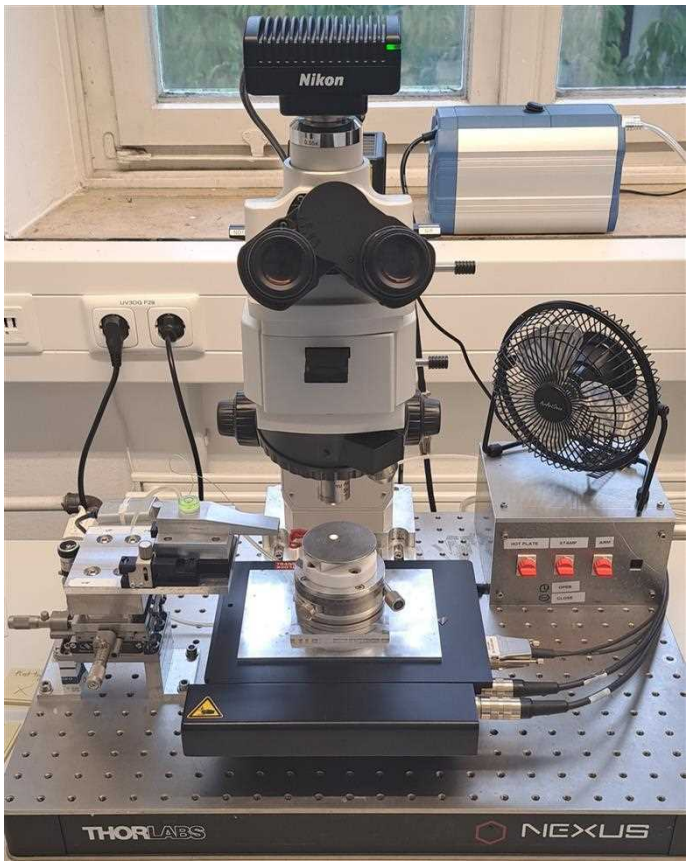

Figure 3.4: Transfer stage overview. Upper stamping stage with glass slide holding vacuum cantilever (left) and lower heated substrate stage (center).

Before we can begin the stacking, we first prepare a stacking plan which involves compiling all viable flakes and comparing their size and shape. We then cut our selected graphene flake in half which is necessary to precisely know and control the twist angle of our two graphene layers in the final stack. There is no known alternative way of precisely relating the crystallographic orientation of two independent flakes with each other. The two main cutting methods either involve the use of a high-power 1064nm laser or an atomic force microscopy (AFM) tip on a glass slide/PDMS assembly to burn or scratch a $\sim$1 µm wide gap into the SLG flake. Additionally, the AFM tip can also be utilised to push away any unwanted crystal fragments or dirt near our stacking material by using the precise stage micromanipulators. This leads to a much smoother wave-fronts during the pick-up process

down the line.

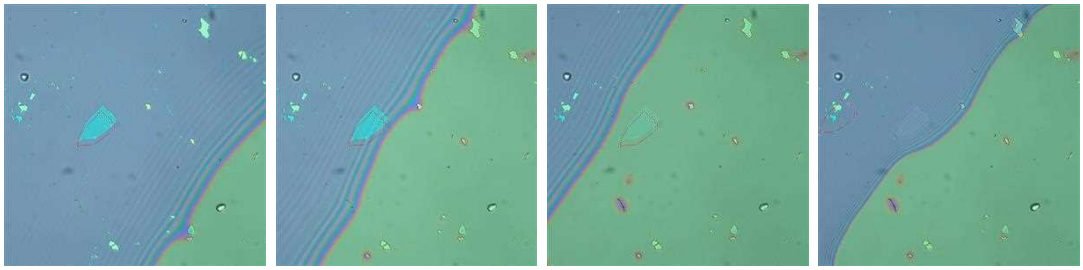

(a) **(b)** **(c)** **(d)**

Figure 3.5: Images of top h-BN pickup process a) & b) Wavefront approaching the crystal, where the contact area is visible through the change in colour, c) Stamp in contact with the h-BN flake, d) Receding wavefront and successful Lift-off of h-BN flake.

We begin the stacking by placing the first silicon chip with the straight edge h-BN crystal on the bottom stage and heat it to $95 - 120$°C depending on stamp quality. The stamp is then attached to the upper stage via a cantilever vacuum system. Before fully lowering the stamp, we first adjust the angle of approach. This is highly important as we want to avoid making contact with the entire substrate all at once and instead have one corner of the stamp touch down first. As soon as contact is established, there is a stark difference in colour and we can observe a wave-front with Newton rings at the transition line. With further lowering we can precisely control the size and spreading speed of the contact area. The wavefront is gently pushed across the substrate until the flake of interest is fully engulfed and then moved back across the crystal in one smooth motion 3.5. At this step, large dirt particles and thick flakes can cause the wavefront to get temporarily stuck and then rapidly snap forward which complicates the process. A loss of colour due to lack of Bragg-shift indicated that the pick-up was successful and the stamp can be fully raised. Due to their transparency, it can be quite difficult to identify flakes once on the stamp, so it is important to keep track of their position.

The used exfoliation substrate is then discarded and exchanged for our pre-cut graphene sample chips. The next round of stacking remains quite similar, with the distinction that this step requires careful alignment of the silicon substrate. We make use of the well-defined edge of the initial h-BN and line it up with the gap in-between the two graphene pieces. We can then pick up the first SLG crystal, rotate the bottom stage by $\theta = 1.1^\circ$ and then lift the second piece of graphene. In the optimal case, both graphene flakes extend slightly beyond the h-BN on at least one side. This causes them to fold around the top h-BN layer during the pickup process, also known as clamping which secures the relative crystallographic orientation of the graphene and significantly reduces the risk of relaxation. During relaxation the small metastable twist between the SLG layers relaxes back into the aligned A-B graphene configuration which proves detrimental to our efforts to generate correlated materials.

To finish the stack, we then pick up the second (bottom) h-BN as well as our bottom graphite gate. It is essential, that there exists no direct contact between graphite and graphene as this would short our gate and essentially render our device useless.

The complete stack is then deposited on a pre-patterned 40 electrode chip by making contact with our stamp and then increasing the temperature to above 150°C. This causes a gradual reduction in viscosity in the PC until it detaches from the PDMS cushioning. If we now lift the stamp, the stack as well as the melted PC will remain on the substrate chip. The stacking is completed by submerging the sample in Chloroform, Acetone and IPA for two minutes each to dissolve the PC film as well as any other contaminations. The final 2D material heterostructure on a contact-electrode waver is depicted in Figure 3.6.

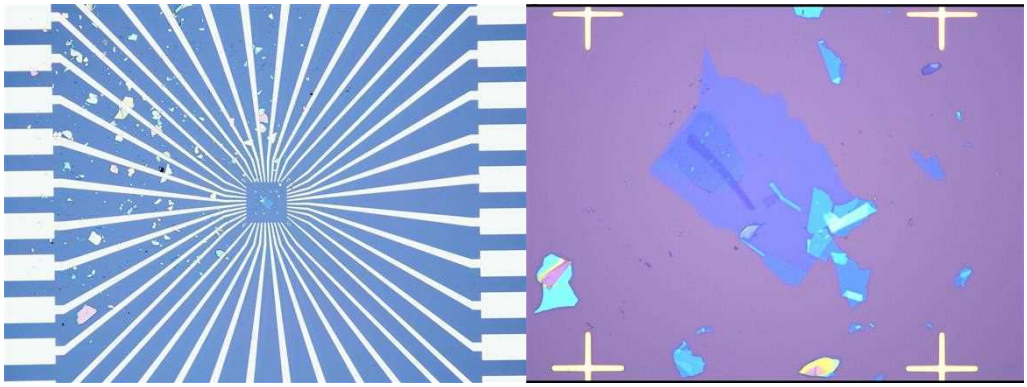

(a) **(b)**

Figure 3.6: Finished stack on electrode chip a) Overview of the entire chip with outer wirebonding pads and connection paths. b) Enlarged image of the central region with a deposited stack. The distance between the gold alignment markers is 100 µm.

3.3 Lithographic Device Manufacturing

In order to turn a rough crystal stack into a functional nanodevice, we employ electron beam lithography, plasma etching, as well as evaporative metal deposition.

This is done by spin-coating an electron beam sensitive resist polymer (PMMA AR-P 679.04 950K) at 4000 rpm for 1 min onto our sample chip which creates a ≈270 nm thick coating. We create a device shape in the pattern design program KLayout (Figure 3.7a) and then employ our E-line electron microscope system to inscribe this pattern onto the polymer coating with a dose of 270 $\mu C/m^2$. During the following 55s development in a 3:1 IPA:4-methylpentan-2-one solution, all exposed regions fully dissolve and leave a resist nanostructure behind (Figure 3.7b). The high precision electron beam allows us to create well-defined features well below 1µm.

Our sample is then further processed in a SENTECH SI 500 ICP-RIE plasma etching system which generates ionised gas, consisting of a combination of 40 sccm HCF_3 and 4 sccm O_2 at a pressure of 90 mTorr. After $\sim 1-2$ min depending on h-BN thickness, all exposed areas will be completely devoid of any 2D crystals and we are left with our desired hallbar structure.(Figure 3.7c)

The PMMA resist pattern is then dissolved via submersion in acetone and IPA for ~ 2 min each and the lithography process is repeated to create on-chip contact wires

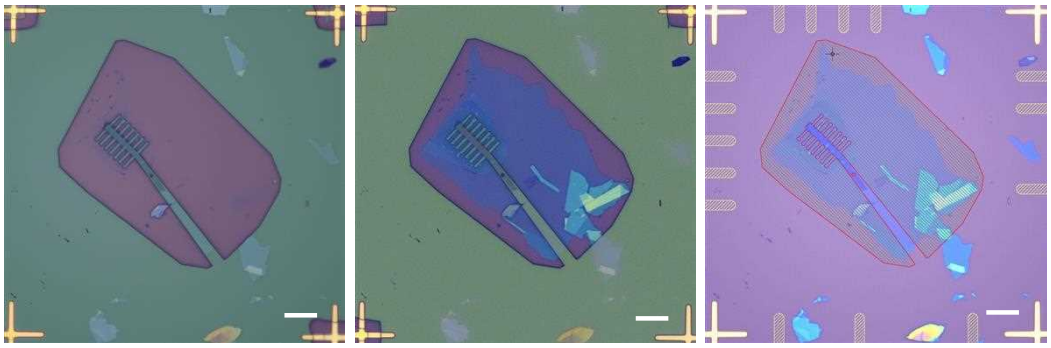

(a) **(b)** **(c)**

Figure 3.7: Fabrication of hallbar device shape a) Design of device in Klayout. b) E-beam resist after exposure. c) Etched hallbar shape with resist still attached. 10 µm scale-bar in white.

to the outer contact pads (Fig. 3.8 a) & b)). The etching time is reduced as we are only aiming to access the graphene layers. The material of choice is gold, as its combines high conductivity with chemical inertness. It is deposited via a ultra-high vacuum electron beam evaporator with a total thickness of 50nm and an additional 5nm of chromium below for better adhesion.

As a result the entire sample, both regions with and without resist, are covered in a homogeneous film. To initiate the lift-off process, we submerge the substrate in 50◦ C hot acetone for at least 3 hours which dissolves the PMMA. Only material that was directly deposited on the exposed sections of the chip will remain attached while the rest will begin to float. By inducing some flow within the acetone beaker, the suspended gold detaches and we are now left with well defined metal contact in the shape of our previous exposure (Figure 3.8c). The contact itself generally takes place at the edge of a stack forming a so-called 2D contact with typical resistances of $\sim 1 - 5$ kΩµm.

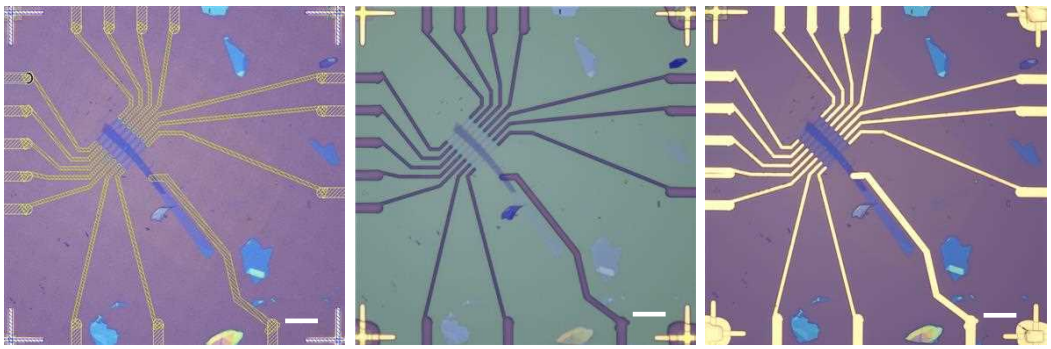

(a) **(b)** **(c)**

Figure 3.8: Creation of gold contactsa) Klayout design. b) Exposed resists. c) Finished device after lift-off. 10 µm scale-bar in white.

3.4 THz Antenna

A very important factor for accomplishing THz transport experiments on 2D nanodevices is their electromagnetic cross-section at the relevant wavelengths. In the range around 1 THz, transmittance measurements of single layer graphene on a Si/SiO_2 substrate show an absorption of only 2-3 % [14]. Paired with the small device size $\sim$ 10 µm - 20 µm relative to the wavelength $\sim$ 0.3 mm (at 1 Thz) this leads to an extremely small radiation cross-section. Additionally, the total output power of our photomixer is limited to below 2 µW [49] and it is therefore extremely difficult to measure the THz response of graphene heterostructures at these conditions. To combat these issues, extensive efforts were undertaken by our group to design, simulate and fabricate on-chip antennas that funnel the incident radiation into our devices [23]. For this purpose, we choose a bot-tie antenna shape. It provides a broad-band impedance, high radiation funneling and its simple shape is compatible with our previous electrode chip designs. Its similarity to a dipole antenna also provides a quick estimate for its resonance frequency f_{res} based on the antenna length L:

$$f_{res} = \frac{c}{\lambda_{res}} \lessapprox \frac{c}{2L} \tag{3.1}$$

For optimising the antenna performance at specific resonance frequencies (0.5 / 1 THz), simulations using COMSOL were performed. Geometric parameters like size, opening angle and gap length were explored with the goal of maximising absorption together with minimizing the impedance mismatch between the bow-tie and the MATBG sample. Gold presents an easy choice of material, as its high conductivity and absorption in the THz spectrum are ideal. In the typical height range of lithographic nanostructures $\sim$ 50 nm, it effectively acts as a perfect absorber. The functionality of the antenna is therefore not significantly altered by changes in vertical cross-section. The resulting design combines both antenna and contacting electrodes on a pre-patterned waver is depicted in Figure 3.9

The design is then lithographically manufactured on an empty 285 nm $Si/Si0_2$ waver similarly to the electrode evaporation in the previous section. The only variation is the use of AZ 5214 E photoresist and our Heidelberg Instruments µMLA photolithography system. The exposure is hereby achieved via ultraviolet light and trades a significantly increased speed for a worse minimum feature size compared to e-beam lithography. In this case this is not of concern for us, with the smallest features possessing a size of 1 µm and the maximum resolution of µMLA being 0.6 µm [21].

The finished antenna substrates are then used in a similar manner as the default 40-electrode wavers. To be more precise, the finished stacks are dropped in the center, and then fabricated via e-beam lithography (Figure 3.10). Notable is that the antenna arms are also extended during this process and provide an additional pair of measurement contacts.

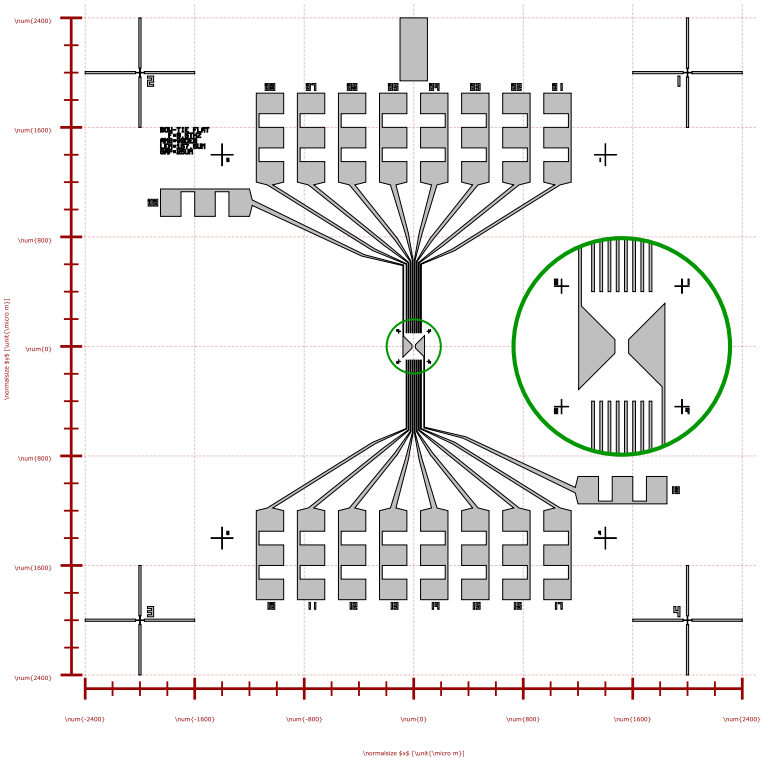

Figure 3.9: Final antenna design with f_{res} = 0.5 THza) Full mask overview with a total size of 4800 µm x 4800 µm. Figure displays enlarged depiction of label and central antenna section as well as the final bow-tie parameters in blue. Final design iteration by C. Hudeczek [23].

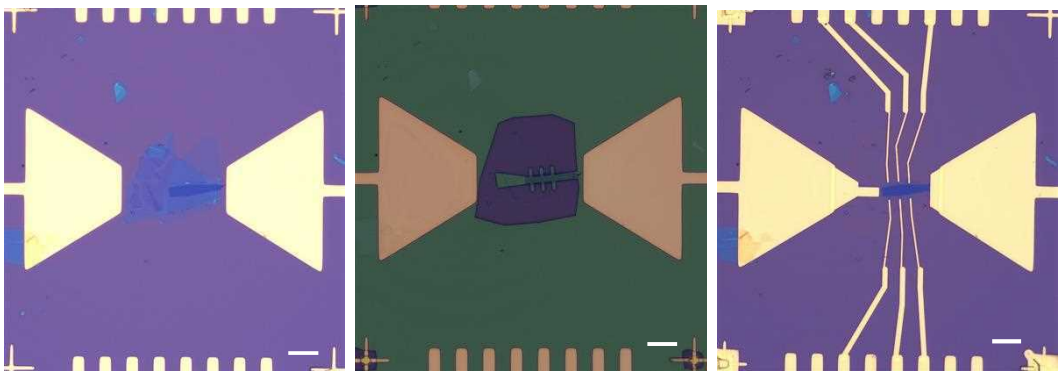

(a) **(b)** **(c)**

Figure 3.10: Fabrication of SLG device on antenna chip. a) Stack after being dropped on substrate. b) Device shape defined by e-beam lithography and etched. Resist not yet removed from the sample. c) Finished device after lift-off, the initial positioning of the stack was sub-optimal, therefore the asymmetric antenna arms. 10 µm scale-bar in white.

Chapter 4

Experimental Methods

4.1 Dilution Refrigeration Cryostat

The observation and measurement of correlated states and quantum effects require extremely low temperatures < 1 Kelvin as phonon induced disorder proves detrimental to their coherence. Therefore several refrigeration techniques for reaching the milli-Kelvin range have been devised. In the course of this thesis we will focus on one particular method, dilution refrigeration (DR). It consists of several stages displayed in Figure 4.1a, with consecutively lower temperatures down towards the sample stage at 30 mK. During operation it is also enclosed by 3 layers of metal shielding ensuring appropriate vacuum and thermal shielding.

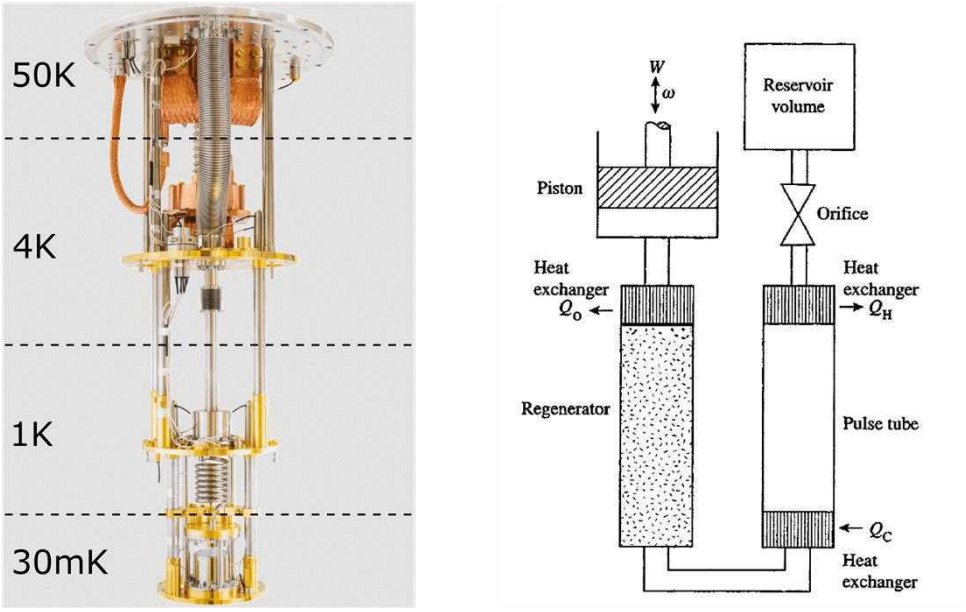

(a) **(b)**

Figure 4.1: Bluefors dilution refrigerator and pulse tube pre-cooler a) Different DR stages depicted without vacuum chamber and thermal radiation shields [8]. b) Schematic of a simple single-stage Pulse Tube cooler. Image adapted from [37].

4.1.1 Pulse Tube Pre-Cooler

A dilution refrigerator uses a pulse tube pre-cooler (PTC) at the initial stages in order to reach a temperature of 4 K. PTCs are often the preferred choice as they combine high efficiency with excellent reliability due to the lack of moving parts at cryogenic temperatures [2].

It operates by creating oscillating pressure waves within ^{4}He Gas, schematically depicted in Figure 4.1b. This flow is directed trough a heat exchanger at its upper ambient-temperature end to remove any heat from the initial external compression (Q_0). It then passes through a regenerator filled with a porous, heat-storing material. At its lower cold-end it is connected to a tube with a valve orifice restriction at its upper, warmer end. During high-pressure phases, compression heat (Q_H) is generated at this end and removed by another heat exchanger. The subsequent low-pressure phases lead to gas expansion within the pulse tube and therefore cooling Q_C at its bottom heat exchanger. The available cooling power of this crude design can be improved in several possible ways ranging from the introduction of additional stages and inlets at the pulse tube [47] to the optimisation of compressor frequency and reservoir volume [37]. Employing these innovations, the modern PTC typically used in DR systems reach cooling powers of 1-3 W at 4.2 K [9].

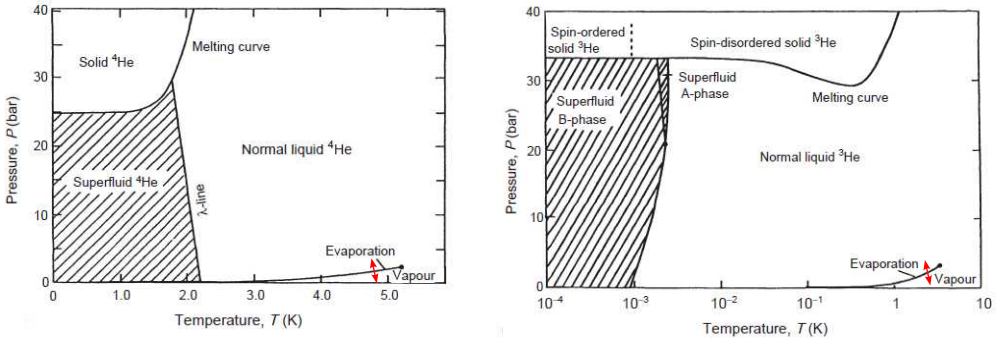

(a) **(b)**

Figure 4.2: Phase Diagrams of Helium a) ^{4}He and b) ^{3}He with the evaporation transition marked in red [37].

4.1.2 Evaporative Cooling

In order to achieve even lower temperatures, methods involving adiabatic compression/expansion of Helium gas loose their viability. Instead, cryostats relying on the phase transition during evaporation of liquid ^{4}He are capable of reaching 1.3 K or even down to 0.3 K in the case of ^{3}He [37]

The exponential decrease of vapor pressure with lower temperatures (L being the latent heat of evaporation),

$$P_{vap} \propto e^{-L/RT} \tag{4.1}$$

and the subsequent increasingly narrow vapor phase in Figure 4.2 show that evaporative cooling is not capable of reaching temperatures in the low milli-Kelvin range.

Therefore a new method, dilution refrigeration, was devised which can achieve temperatures well below 300 mK.

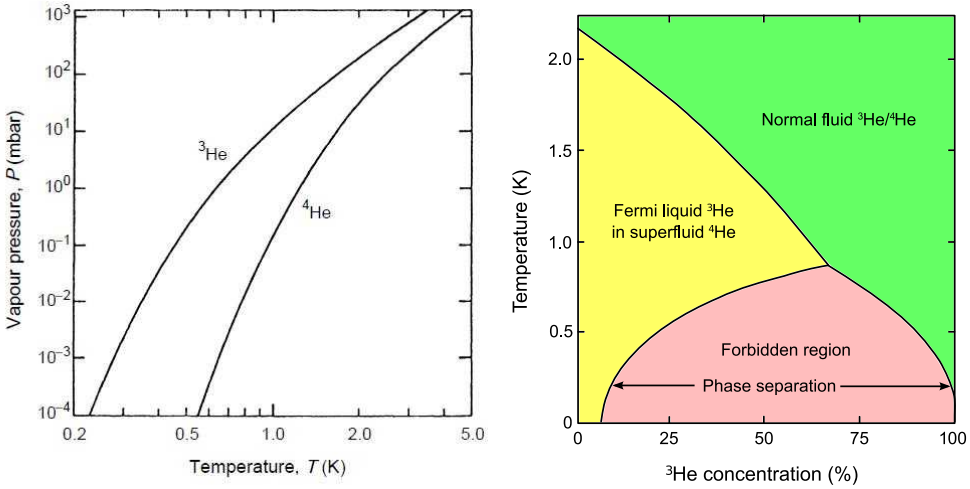

(a) **(b)**

Figure 4.3: Vapour pressure of ^{3}He ^{4}He and phase diagram of ^{3}He-^{4}He mixtures Figures adapted from [37].

4.1.3 Dilution Process

The fundamental principle of a dilution refrigerator, is the spontaneous phase separation of liquid ^{3}He - ^{4}He mixtures below 0.87 K into a ^{3}He-rich and a ^{3}He-poor phase, with the ^{3}He-concentrated phase floating on top due to lower density.

What makes this process so interesting for cryogenics, is the fact that the rich phase purely consists of ^{3}He while the dilute phase is 93.4% ^{4}He and 6.6% ^{3}He. When inducing a flow $\dot{n}_3$ of ^{3}He from the concentrate to the dilute phase, cooling power is generated from the heat difference during mixing,

$$\dot{Q}\dot{n}_3[H_d(T) - H_C(T)] \tag{4.2}$$

with the enthalpy of each phase calculated from the specific heat $C(T)$.

$$H(T) - H(0) = \int_0^T C(T)\, dT \tag{4.3}$$

The experimental values of $C(T)$ compiled in Figure 4.4a show an almost constant specific heat at temperature below 10 K.

From this we can extract specific heat value of pure ^{3}He as $C_3 = 22T$ [J(molK)$^{-1}$] and calculate $C_3(6.6\%) \simeq 106T$ [J(molK)$^{-1}$]. Inserting these parameters into equation 4.2 and 4.3 (A full derivation and calculation can be found in [37]) then leads to a relation for the cooling power only dependent on the flow rate $\dot{n}$ in moles and temperature,

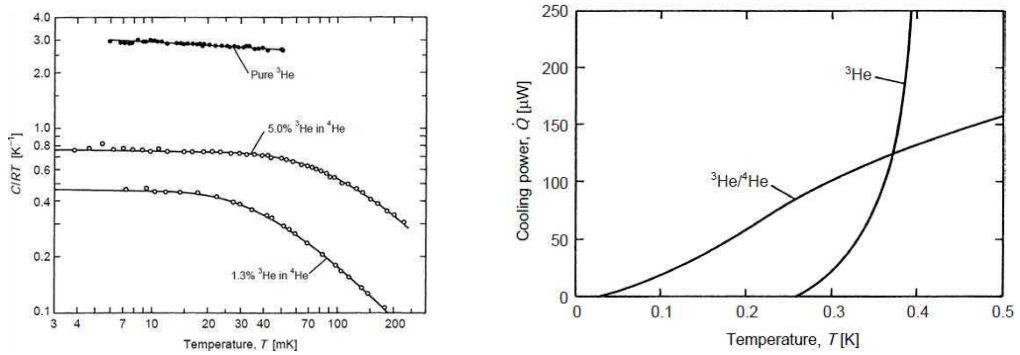

(a) **(b)**

Figure 4.4: Specific heat of ^{3}He at different concentrations and cooling power comparison a) ^{3}He in a mixture approaches a finite specific heat in the limit of low temperatures. b) As a result, the ^{3}He-^{4}He mixtures cooling power at ultra low temperatures is significantly larger than other traditional methods. Both images taken from [37].

$$\dot{Q} = 84\dot{n}_3 T^2 \ [W] \tag{4.4}$$

This quadratic dependence on temperature demonstrates why the dilution process can reach significantly lower temperatures than traditional evaporative cooling with an exponential decrease in cooling power shown in Figure 4.4b. With standard values for our Bluefors DF of $\dot{n}$ =0.4 mmol/s and T=45 mK we reach values of $\dot{Q}$ =68 μW.

With this knowledge, one can construct a working dilution cycle as seen in Figure 4.5 consisting of [54]:

- The circulation pumps (typically a turbo and scroll pump) at room-temperature create high pressure within the ^{3}He gas circulating in the system, which is then pre-cooled in several steps at the 50 K and 4 K stages.
- At this point the ^{3}He is still gaseous before it enters a condenser and a subsequent flow impedance. They provide the sufficiently low temperature $\sim$ 1.5 K and required pressure (30 - 200 mbar) for condensation to take place [37].
- Before the liquid helium can continue down toward the mixing chamber, its path is restricted by a second impedance that prevents reevaporation.
- It now passes through a counterflow heat-exchanger before reaches the top of the mixing chamber.
- This is where the previously discussed dilution process is taking place, with ^{3}He atoms moving trough the boundary between the two phases to dissolve into the lower ^{3}He-^{4}He mixture while pulling thermal energy from the environment.
- Due to osmotic pressure, the ^{3}He atoms within the diluted phase move back upwards through the previous heat-exchanger while cooling the incoming pure ^{3}He-liquid.

- In the still chamber, the low pressure created by the rear end of the circulation pump induces evaporation.
- Additionally, a small heater ∼10 - 15 mW is attached to the still chamber. We can use it to increase the evaporation and therefore the cooling rate.
- However, the heater itself also introduces thermal energy into the system, so raising it beyond 15 mW has a negative impact on the achievable DR base temperature. For our cryostat, the optimal value lies in-between 10 - 12 mW, depending on the setup configuration.
- Highly important during the evaporation process is the large difference $\sim 10^3$ in vapour-pressure between ^{3}He and ^{4}He as seen in Figure 4.3, so that even at low concentrations of ^{3}He in the mixture, the resulting gas consists almost exclusively of ^{3}He.
- The higher concentration of ^{4}He atoms that remain in liquid are then responsible for the previously mentioned osmotic force while the ^{3}He are re-compressed to close the cycle.

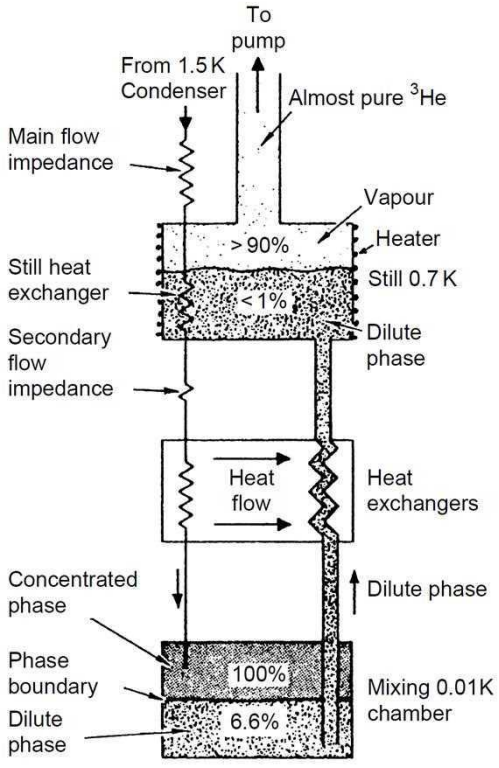

Figure 4.5: Basic dilution process schematic. The percentage values hereby indicate the ^{3}He portion within the different phases. Pumps and heat exchangers at higher stages and RT not depicted. Image from [37]

4.1.4 Cooldown Process

After covering the basic operating principles of a DR, we will focus on the cooldown process from room-temperature while elaborating on important technical details:

- We begin with a DR system in the default offline state, no shielding attached, the inner core exposed and the ^{3}He-^{4}He mixture stored in an external tank for safekeeping. All setup modifications, troubleshooting and sample loading needs to be finished due to inaccessibility later on.
- The different layers of shielding and the SC sample magnet (for magnetic transport measurements detailed in Chapter 5) are successively mounted and secured with screws. While the inner layers are only responsible for shielding thermal radiation, the outer most canister also needs to provide a good vacuum seal and is therefore cleaned with IPA before mounting.
- The cold-trap located outside of the DR is submerged in liquid nitrogen. This is an important component within in the ^{3}He-cycle located after the circulation pump(s) and is responsible for freezing-out any impurities that might enter the mixture.
- The inside of the vaccum cannister as well as most of the internal gas handling lines are pumped to a pressure below 10^{-4} mbar while avoiding an open path to the He-mixture filled sections in order to prevent loss of the mixture.
- The cryostat is now ready for cooldown which is begun by initiating the ^{4}He pulse tube pre-cooler. The system will now gradually cool from 300K down to 4K which takes approximately 24 hours.
- As soon as the temperature stabilises, the dilution process is initiated. The gaseous ^{3}He-^{4}He mixture is injected into the dilution cycle from an external tank which leads to an initial spike in temperature visible in Figure 4.6. As soon as the pressure in the loop increases, the ^{4}He starts condensing at the still stage. By pumping on the liquid ^{4}He and inducing evaporation the DR cools down to 1 K.
- At this point the temperature is low enough for the ^{3}He to liquefy too and using evaporative cooling like before, the system reaches 300 mK.
- This is where the dilution process takes over and after an additional $\sim$ 3 days it will reach a base temperature of 30 - 40 mK.

4.2 Electronic Transport Measurements

Our transport measurements on MATBG hallbar structures are performed in a 4-probe configuration where a specific current, usually in the range of 10 - 20 nA, is sent through two outer contacts while analysing the potential drop-off at a second pair of intermediate contacts. We can also study the orthogonal voltage via 2 additional contact points. This allows us to accurately obtain the sample resistivity as there is essentially no current flowing through the measurement arms and therefore contact resistance between our sample and wiring is neglectable. On top of that, high sensitivity electronic transport measurements at extremely low temperatures require us to minimise thermal noise as well as externally induced heating within our sample. For this purpose, we utilise several important methods including Lock-in amplifiers,

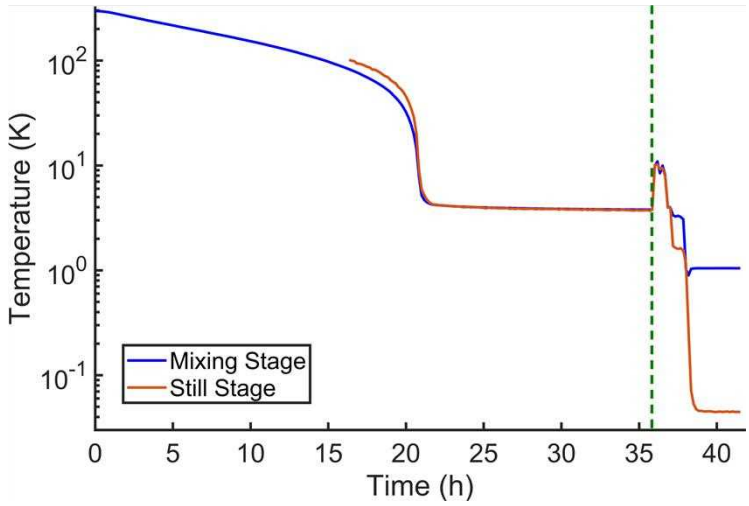

Figure 4.6: Temperature evolution during cool-down process. Curves measured from cryo-compatible thermometers at the still (orange) and mixing (blue) chamber stages where the vertical green line indicates the initiation of the dilution process. Missing data from the orange graph is due to a limited thermometer range of < 100 K

thermalised cryogenic wiring and electronic filtering, which will be discussed in this section.

4.2.1 Lock-in Amplifiers

A lock-in amplifier operates by imposing a periodic, low-frequency (typically $<$ 50Hz) signal on the measurement via the outer current biasing. The resulting response is then multiplied with the fixed reference and subsequently passed through several low-pass filters. This phase-sensitive detection only extracts signals in a small frequency window around the initial reference while removing undesired noise with random frequency components. This significantly boosts our available signal to noise ratio [32].
The Standford Research SR860 lock-in amplifiers that were utilised for most measurements in this thesis simultaneously applies two separate modulations, with the second one begin shifted by 90°. The result is one in-phase and one out-of-phase channel, named X and Y and from this, the total amplitude R as well as the overall phase offset θ can be obtained [33]:

$$R = \sqrt{X^2 + Y^2} \qquad \theta = arctan(Y/X) \tag{4.5}$$

4.2.2 Cryogenic Wiring

The wiring that connects our samples in the DR all the way to the measurement electronics located at room-temperature opens up two new pathways for thermal leakage into our system. The first one involves direct thermal conduction in between elements of different temperatures T_1 and T_2 which is described by [15]:

$$\dot{Q} = K(T)A\frac{dT}{dx} = \frac{A}{L}\int_{T_1}^{T_2} K(T)\,dT \tag{4.6}$$

via the thermal conductivity $K(T)$, wire cross section A. We therefore require a wire material that minimises $K(T)$, particularly at low temperatures. One can easily see that standard copper wiring is thus unfit for this purpose and instead, SCuNi-CuNi based coaxial cables with a thermal conductivity of $7.1 \cdot 10^{-5}$ Wcm/K [10], orders of magnitude smaller than copper, are used. Additionally, the cables are thermalised at every stage to minimise the thermal load for the lower stages.

4.2.3 Electronic Filtering

As a second measure of temperature isolation, we also need to limit the thermal energy of the individual electrons within our sample. Similarly to lattice vibrations of nuclei (phonons), electrons possess an inherent temperature (T_e), which manifests within a conductor as high frequency electromagnetic oscillations $h\nu = k_B T$. In systems that reach equilibrium, the electronic and lattice temperature (T) will always ultimately equalise, but due to the current flow passing through different temperature stages, this is clearly not the case here. We therefore require heavy filtering with a cut-off frequency of <630 MHz for $T_e = 30$ mK This is achieved via two low-pass filters, with a RC-filter (65 kHz) at the 1K stage and a RF-filter (225 MHz) at the mK stage.

Chapter 5

Implementation of Terahertz milli-Kelvin Setup

Performing Terahertz transport measurements on superconducting MATBG requires sample temperatures well below the critical transition temperature T_C. For this purpose, we established a custom setup within our Bluefors dilution refrigerator. Central for these efforts is the efficient generation of THz radiation.

The THz emission for our experiment needs to take place locally within the DR for two main reasons:

- Even though Terahertz fiber technology has recently seen immense advances, its is not yet at the stage of applicability within a cryostat. [24]
- Black-body (BB) radiation generated by THz components at RT and intermediate DR stages can interfere with experiments. The sample needs to be shielded particularly from the 50K stage with a BB peak frequency of $f_{Peak} \sim 5$ THz.

For this purpose, photomixers offer ideal properties due to their small size, large spectral range, low heat generation and cryo compatibility.

5.1 THz Generation via Photomixer

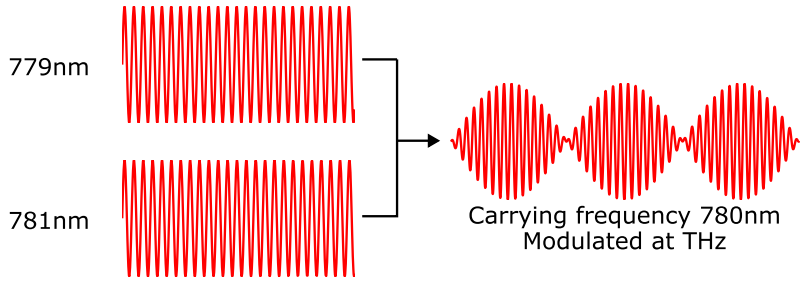

Figure 5.1: THz Beatwave generated from two Lasers.

The operating principle of this emitter is based on two continuous-wave (CW) diode lasers in the near-infrared (NIR) located outside of the DR driving the photomixer within. The lasers are stabilised by a grating structure, restricting the emissions to a single longitudinal mode and creating a very narrow emission frequency. We can modify the grating pitch width, and therefore the wavelength via the laser temperature. During operation, the two lasers are slightly detuned and when superimposed in a mixing fiber, the resulting emission experiences an oscillating intensity.

The intensity and repetition rate are determined by strength and relative frequency offset of both lasers (with m describing the quality of laser overlap):

$$P(\omega_{THz}, t) = P_1 + P_2 + 2\sqrt{mP_1P_2}cos(\omega_{THz}t) \qquad \omega_{THz} = 2\pi\nu_1 - \nu_2 \tag{5.1}$$

The resulting beat wave is then transmitted into the DR via a simple optical fiber reaching down to 1 K stage where the photomixer itself is located. It consists of a galium-arsenide substrate with a gold nanostructure lithographically deposited on top and a silicon lens below as seen in Figure 5.3a. The photons that are absorbed by the semiconductor substrate possess enough energy ∼1.59 eV for 780 nm to excite electrons across the band gap ∼1.43 eV at 300 K and 1.52 eV at 0 K [27] and generate free charge carriers n [19]:

$$\frac{dn}{dt} = \frac{\eta}{h\nu Ad}P(\omega, t) - \frac{n}{\tau} \tag{5.2}$$

Hereby, η is the external quantum efficiency while A and d describe the absorption area and depth. τ signifies the mean charge carrier lifetime. Solving this differential equation then results in the following time-dependent carrier density [19]:

$$n(\omega, t) = \frac{\eta(P_1 + P_2)\tau}{h\nu Ad}\left[1 + \frac{2\sqrt{mP_1P_2}}{P_1 + P_2}\right] \times \left[\frac{\omega\tau sin(\omega t) + cos(\omega t)}{1 + (\omega\tau)^2}\right] \tag{5.3}$$

When adding external bias to the gold formation (in our case up to 5V), current can only flow when there is sufficient laser intensity to generate free charge carriers. This leads to an oscillating current at THz frequencies within the antenna and substrate. The acceleration and deceleration of charge carriers during this process lead to electromagnetic emissions at ω_{THz} [38].

In order to describe this process we consider the equivalent circuit of the photomixer (Fig. 5.2) which possesses an intrinsic capacitance due to the GaAs - gold interface as well as an antenna resistance R_A. After approximating the resulting conductance of the photoconductive gap with the effective carrier mobility μ and the gap width r,

$$G(\omega, t) \approx \frac{\mu ed\sqrt{A}}{r}n(\omega, t) \tag{5.4}$$

We follow Gregory et al. [19] to calculate the electrical power being dissipated into the antenna. The time dependent THz component is hereby:

$$P_A = 2\frac{R_A V_B^2}{A}\left[\frac{\eta\mu e\tau}{rh\nu}\right]^2 \frac{mP_1P_2}{[1 + (\omega\tau)^2][1 + (\omega R_A C)^2]} \tag{5.5}$$

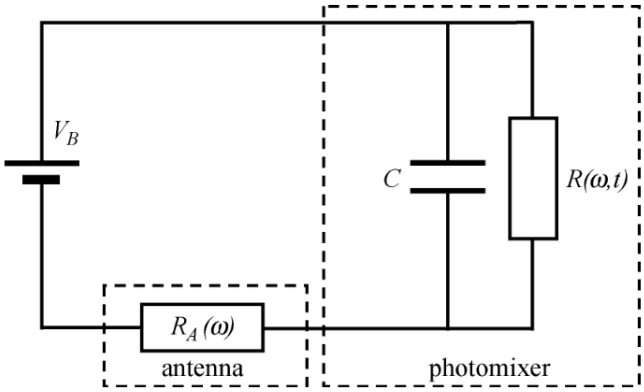

Figure 5.2: Equivalent circtuit of a photomixing emitter Figure adapted from [19]

This does not directly describe the emission power due to imperfect coupling as well as other electric losses, but we can still assume: $P_{THz} \propto P_A$. Therefore we can determine essential factors for optimizing THz power. Interestingly, the power of photomixers drops off at higher frequencies both due to finite charge carrier recombination time as well as device capacitance. In order to maximise emission at a given frequency, we need to boost both laser powers and their overlap. Additionally, the capacitance and gap-size need to be minimised via the antenna design. This is also the reason for implementing small fingers in the antenna gap seen in Figure 5.3b. Depending on the desired frequency range and polarisation, the overall antenna size and shape can differ vastly. In our photomixer it is a log-spiral design Figure 5.3b which offers excellent spectral range from 0.5 THz up to 2 THz as well as circular polarisation.

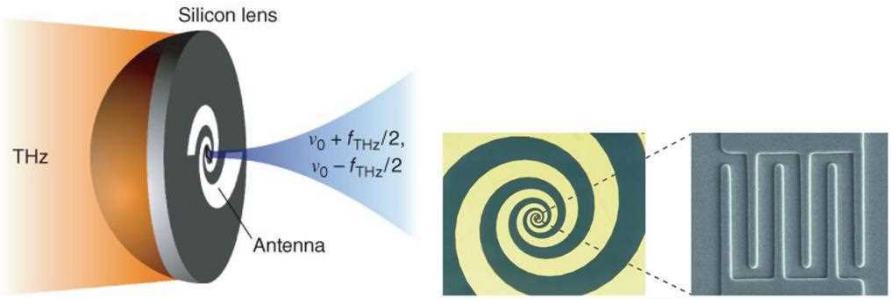

(a) **(b)**

Figure 5.3: Depiction of a Photomixer a) Schematic overview of a complete device (without biasing contacts) and incident NIR light (in blue) around central frequency ν_0=780 nm [38]. b) Images of a log-spiral antenna with central region enlarged. Light induced current passes in-between the interlaced fingers of both antenna arms [28].

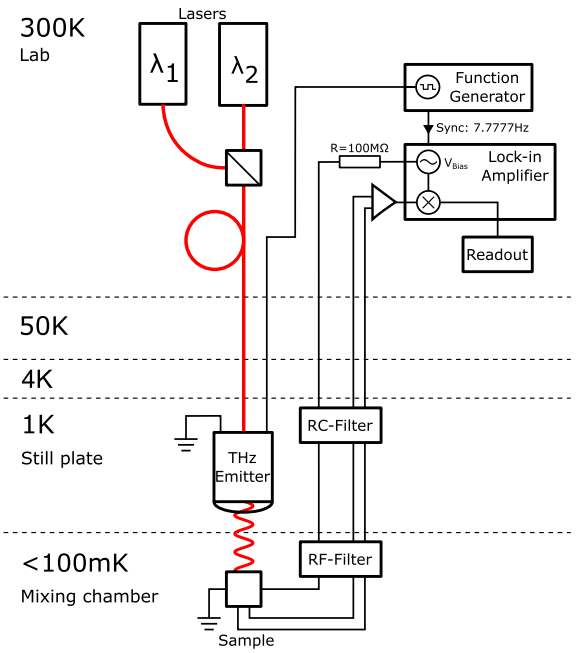

Figure 5.4: Photomixer setup wiring. Depiction of the major components at different temperatures.

5.2 Setup Design

The setup within the DR consists of two main components, the sample- and the emitter stage which were designed in Fusion 360 and subsequently manufactured from high purity oxygen-free Copper (OFC) CW008A plated with 1 µm of Gold. OFC is a high-purity copper alloy with oxygen contents below 0.001 % which is widely used in cyogenics due to its excellent thermal conductivity even at extremely low temperatures. The gold-film also serves two import purposes, both protecting the copper from surface oxidation as well as ensuring a good contact between individual parts due to much a significantly lower surface hardness compared to copper [51]. The individual steps from design to finished components is depicted in Figure 5.5.

5.2.1 Emitter stage

In order to mount and adjust the necessary components, 3 parallel rods are attached to the upper 1 K plate of the fridge. Movable stages which hold the individual THz elements are slid over the optical rails and secured via 3 setscrews which allows for easy height and alignment adjusting. Currently there is only the emitting photomixer attached to this rail system, but its modular nature allows for easy addition of new beam elements like focusing lenses or wave-plates. At the lowest possible position, the sample-emitter distance is only 25 mm, past the typical focal point $f \approx 30$ mm of GaAs photomixers which allows us to reach all possible beam width configurations. The optical fiber and DC biasing line required for the photomixer operation pass through the 1 K plate above the optical stage, see Figure 5.6.
The coaxial cable then connects directly to a breakout panel at the underside of the 4K plate. It is fed into one of our two 24-pin measurement wire bundles that leads

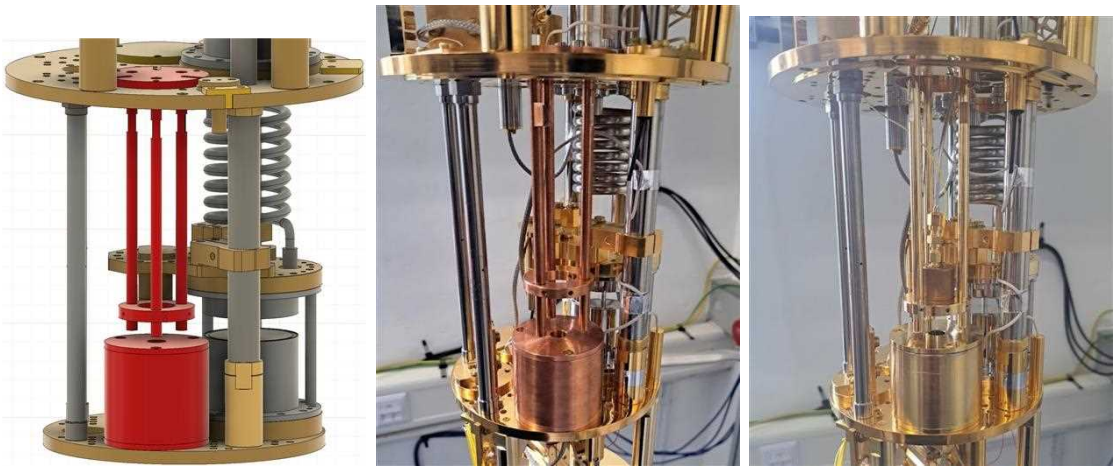

(a) **(b)** **(c)**

Figure 5.5: Setup components in the Bluefors DR a) Snapshot from Fusion 360 with the custom parts in red embedded in an accurate CAD model of our DR provided by Bluefors Ltd. b) Uncoated OFC components during test-fitting. c) Finished components with photomixer installed.

to a function generator at RT used for biasing. We use a square wave profile that is synchronised to the lockin-in frequency of 7.777Hz.
The laser fiber also runs up along the different stages, with several thermo-couplers ensuring proper thermalisation. At the 50K stage, it is patched into a second fiber, that ultimately leads to a laser vacuum feed-through at the very top of the cryostat.

5.2.2 Sample Stage

The sample stage fulfils two essential purposes to facilitate sensitive transport measurements. It provides extensive shielding from thermal radiation as well as a stable electrical connection. It is located on top of the mixing chamber plate centered below the optical stage with a 5mm gap preserving the thermal separation between the 1 K and mK stages.

The TBG chip carriers are held in the center of the sample stage by a contacting socket (Black square surrounding the sample in Figure 5.7 b) which is soldered to a custom printed circuit board (PCB). It connects the central 20 contacts to Cryo-compatible CuNi shielded NbTi wires are running to a 25-pin Microminiature-D connector in the bottom plate of the sample stage. This allows easy disconnection and dismounting of the entire lower stage without affecting the position and alignment of the optical rails above. This is necessary for loading and exchanging samples as there is not enough clearance for the required removal of the thermal shielding can and top plate. When assembled, the shielding almost fully encloses the sample except for a circular 10 mm window in the upper plate right above the sample. Together with a small OFC rod that extends through the PCB and makes direct contact with the sample chip and creates a good thermal connection to the bottom milli-Kelvin plate, the sample can reach temperatures of <50 mK.

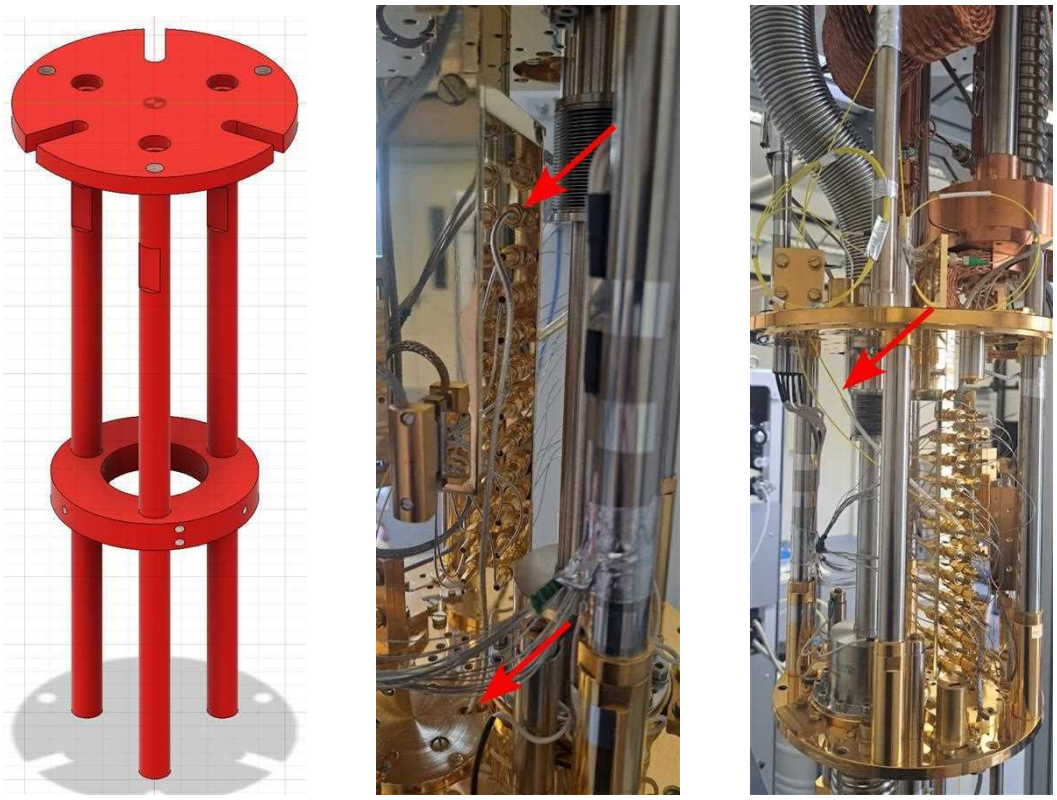

(a) (b) (c)

Figure 5.6: Optical stage design and photomixer wiring a) CAD schematic of the optical rails with one circular stage ring. b) Coaxial biasing wire above the emitter assembly. Red arrows indicate the connection point to breakout panel as well as the feed-through location on the 1 K stage. c) Optical wire leading up to the 4 K stage.

(a) (b)

Figure 5.7: Sample stage a) Schematic of internal components next to thermal shield within CAD-program. b) Image of opened sample stage on custom grounding stand during loading. Sample visible in the center of the golden chip-carrier.

5.3 THz Setup Test

Before the first cooldown, the setup is initially tested at room temperature and under atmospheric conditions to confirm Thz Emission. For this, several different detectors can be utilised, of which a second photomixer is one of the more sensitive and convenient options. It is placed directly below the emitter with a distance of $d \approx 5$cm (Figure 5.8 a). This leads to so-called THz oscillations when sweeping over a range of THz frequencies.

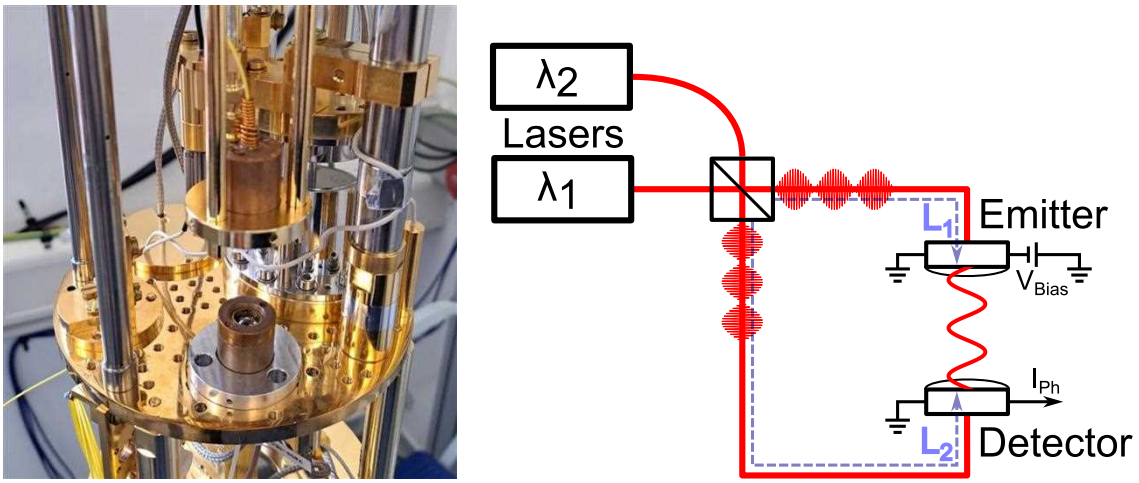

(a) **(b)**

Figure 5.8: Dual photomixer test a) Two photomixers facing each other b) Laser and THz emission form an interferrometric loop.

5.3.1 THz Oscillations

In order to understand the phenomenon of THz oscillations, we first need to analyse the detection process and the origin of phase dependence within the induced photocurrent. In the receiving photomixer, incident THz radiation creates an electric potential:

$$U_{THz} \propto E_{THz} cos(\omega_{THz} t + \Delta\phi) \tag{5.6}$$

For generating any detector signal, free charge carriers are required. We therefore connect the recieving photomixer to the same optical beat-signal as the emitter resulting in a time dependent photocurrent:

$$I_{Ph}(t) \propto U_{THz}(t) P_{THz}(t) \propto cos(\omega_{THz} t) cos(\omega_{THz} t + \Delta\phi) \tag{5.7}$$

Depending on the phase-shift between the incoming THz radiation and the beat-signal, the electric signal possesses a DC component of:

$$\langle I_{Ph}(t) \rangle \propto E_{THz} P_L cos(\Delta\phi) \tag{5.8}$$

This phase shift is ultimately determined by the path length difference $\Delta L = L_1 - L_2$ of the two optical fibres transporting the mixed laser, the gap between the photomixers d and the frequency ω_{THz}:

$$\Delta\phi = \frac{\omega_{THz}}{c}[\Delta L n_{Fiber} + d n_{Air}] \tag{5.9}$$

This leads to periodic oscillations of the generated photocurrent with respect to THz frequency, plotted in in Figure 5.9.

We can then verify the previous mathematical description for our Terahertz emissions, by calculating ΔL from Figure 5.9 and comparing it to the actual length difference between the optical fibers in our setup test. From the data we extract the frequency span of one full oscillation $\Delta\omega$ =166MHz and using refractive indexes of $n_{Fiber} \approx 1.5$ [46] and $n_{Air} = 1$, the calculated path difference amounts to 1.17 m. This comes very close to reality, as during our tests the emitter path L_1 contained an additional 1m of optical fiber as well as a $\sim$ 0.1 m vacuum feed-through compared to L_2.

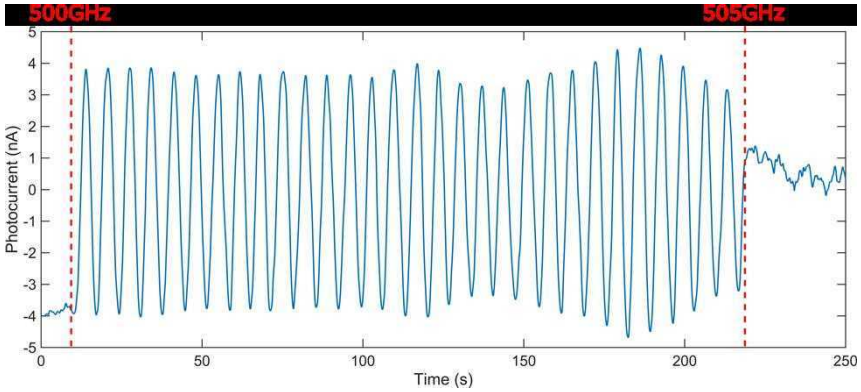

Figure 5.9: Measured THz oscillations. Obtained during frequency sweep from 500 GHz to 505 GHz.

5.3.2 THz Spectrum

We can obtain a relatively accurate representation of spectral intensity by repeating the same measurement over a much larger frequency range and then extracting the amplitude of the oscillations (Figure 5.10). The resulting evolution of spectral power is displayed in Figure 5.11a and it matches the expected decrease with higher frequencies from Equ. 5.5 as well as the data provided by the manufacturer Toptica Photonics AG in Figure 5.11b. Our measurement also includes the slight intensity dips at $\sim$ 1.10 THz and $\sim$ 1.17 THz, originating from absorption peaks of atmospheric water vapor [26].

With these results we can prove the presence of THz emissions and a spectral intensity behaving according to our expectations.

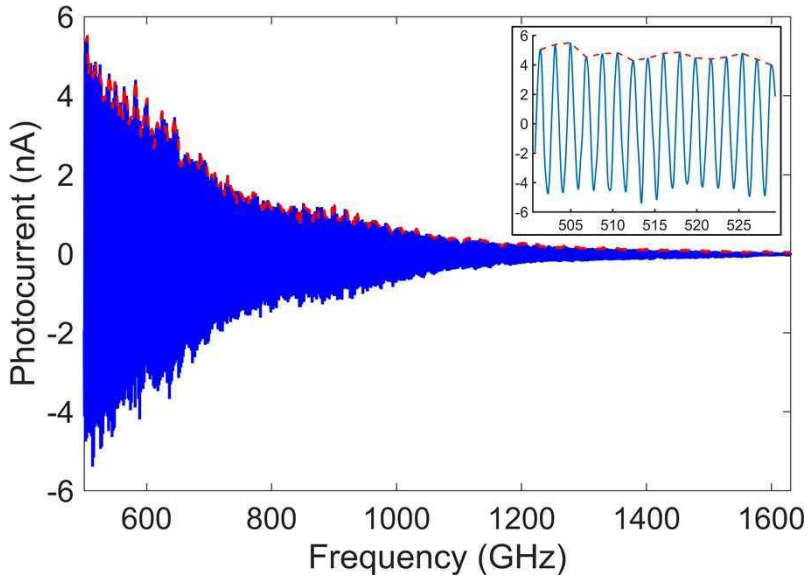

Figure 5.10: Terahertz oscillations Evolution of Amplitude at different frequencies with enveloping curve in red. Enlarged graph of 500 to 530 GHz in the top right.

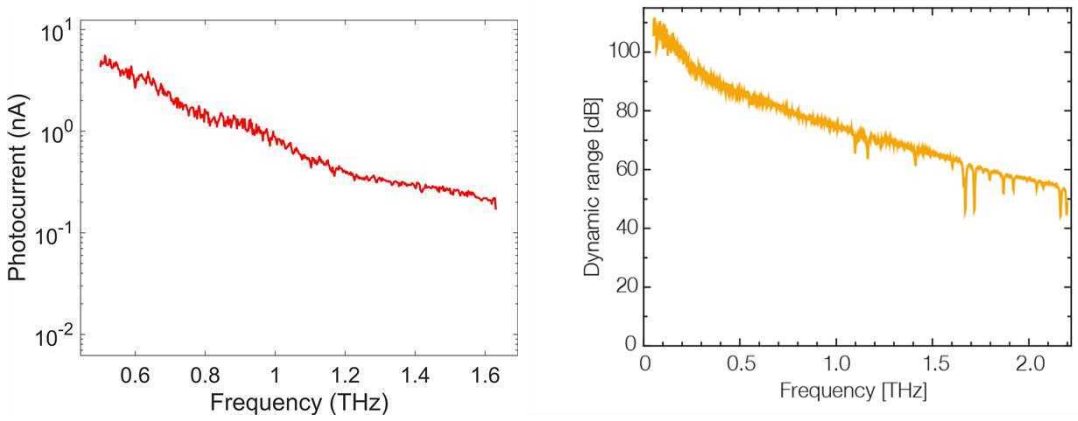

Figure 5.11: THz spectral power. a) Photocurrent extracted from measurement data in Figure 5.10. b) Reference spectrum provided by Toptica Photonics AG [50].

5.3.3 Photomixer Heat Generation

The biggest concern for implement any new equipment or setup in a cryogenic environment is always excessive heat leaks and generation. From the beginning of the designing phase, careful considerations were undertaken to minimize the impact on the achievable DR base temperature. This includes the aforementioned separation of emitter and milli-Kelvin stage, sample shielding as well as thermal isolation. These goals are never perfectly achievable as we will always need some access points to interact with our system. We now perform a cooldown in order to analyse the heating power that is created by the photomixer.
In an idle state, the optical line does not measurably influence the mixing stage temperature due to its low thermal conductivity. The coaxial biasing line on the other hand, creates a noticeable increase in temperature when mounted, a shift at the still plate from 1.05 K to 1.17 K. Even though it has no direct connection

to the mixing stage it can still raise its temperature from 45 mK to 67 mK due to interference with the dilution process and a subsequent reduction in ^3He flow rate by 0.13 mmol/s. With this data, we can confirm that the overall impact lies within acceptable parameters and our new setup components have not introduced any major heat leaks.
At this point, we still need to study the direct heat generation during photomixer operation. Here, the total heating power of the photomixer can be approximated as:

$$P_{tot} = P_{Laser} + P_{Bias} = P_{Laser} + I^2R \tag{5.10}$$

By using a laser power meter as well as previous resistivity classifications of our photomixer ($I \approx 50$ µA, R ≈ 50 kΩ), we find heating contributions of $P_{Laser} \approx 25$ mW and $P_{Bias} \approx 0.125$ mW. The heating from the laser is hereby much more significant than the biasing. This also matches our experimental data, with the extracted DR temperatures during photomixer operation displayed in Figure 5.12. The lasers (which are activated first) increase the temperature by 300 mK and 7.5 mK at the 1K- and mK-stages as well as upping the flow of ^{3}He by 0.03 mmol/s. The effect of the biasing is significantly lower at the still-stage (40 mK) and not noticeable at the mixing stage. Clearly a fraction of the heat produced by the laser is able to reach the lower stage potentially originating from a laser leak which would allow optical light to directly hit the mixing stage. In order to rule this scenario out, we compare the increase in 1K-stage black-body radiation to the cooling power at the new equilibrium temperature. We can use the Stefan-Boltzmann equation to estimate the relative increase of thermal radiation:

$$P_{BB} = A\epsilon\sigma T^4 \qquad P_{rel} = \frac{P_{new}}{P_{old}} = \frac{T_{new}^4}{T_{old}^4} \tag{5.11}$$

From just the lasers (1.08 K → 1.2 K), we receive an relative increase in black-body radiation of $P_{rel} \approx 1.53$. The relative shift in $\dot{Q}$ is given via the change in mixing chamber temperature (66.5 mK → 74 mK) and flow rate (0.24 mmol/s → 0.27 mmol/s):

$$\dot{Q}_{rel} = \frac{\dot{n}_{3,new}T_{new}^2}{\dot{n}_{3,old}T_{old}^2} = \frac{0.27}{0.24}\frac{74mK^2}{66.5mK^2} = 1.39 \tag{5.12}$$

These results ($\dot{Q}_{rel} = 1.39 \approx 1.53 = P_{rel}$) show us, that the increase in cooling power and therefore temperature are closely related to the stronger black-body radiation from the 1K stage. From this relation we can conclude that a significant laser leak is unlikely as it would lead to much higher base temperatures.

In summary, our new setup does introduce some level of heating, but within expected parameters when operating a heat generating emitter. The cryostat still achieves temperatures of <100 mK, well below the necessary critical superconducting temperature T_C. Nonetheless, there is still room for further improvements like filtering and better thermal decoupling of the biasing wire.

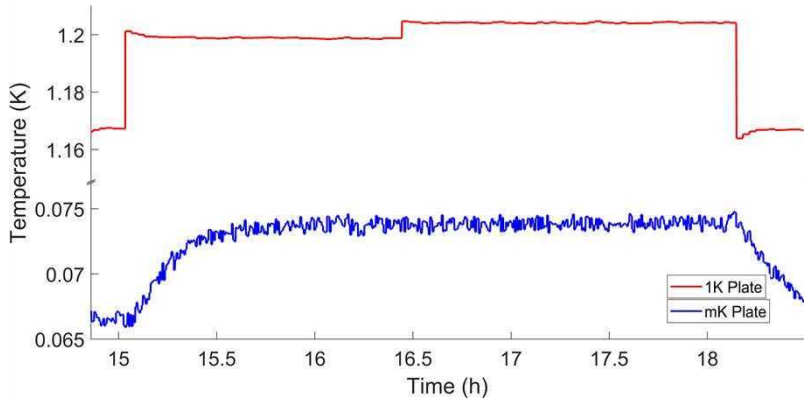

Figure 5.12: Still and mixing plate temperatures during photomixer operation. Beat-wave lasers turned on at t= 15.03 h and bias applied at t= 16.44 h.

5.3.4 Test Measurements via Single Layer Graphene Device

The final test that is required to confirm the validity of our setup is performing an actual measurement on a graphene sample. This initial trial was performed with a SLG, graphite bottom gate device on an antenna substrate with a resonance frequency $f_{res} \approx 0.5$ THz. It is significantly faster and more consistently to fabricate than the highly crystal orientation dependent MATBG. It does however lack the correlated phenomena present in twisted multi-layer graphene.
We follow the device configuration of Vicarelli et al. [52], connecting one arm of the antenna to the SLG and the other to the graphite gate (Figure 5.13). Intermediate contacts along the gap form the familiar hallbar structure that has seen extensive use in previous experiments (Figure 3.10). If we now apply a current across the SLG and a varying potential at the gated antenna, we can test the device by recovering the standard resistive behaviour for graphene (Figure 5.14). It is characterized by a broad resistance peak at the charge neutrality point $V_g \sim 0$ V

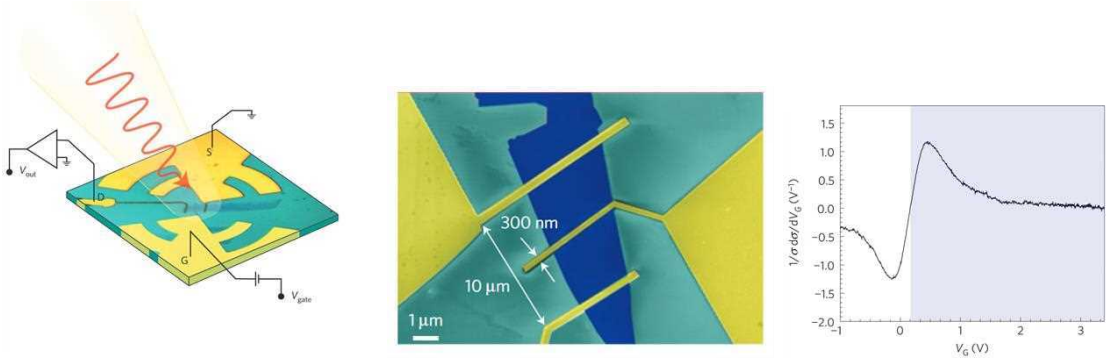

(a) **(b)** **(c)**

Figure 5.13: Single layer graphene THz detector. [52] a) Device design and electrical configuration. b) Enlarged center section with gold gate connected to one of the antenna arms c) Expected response of depicted SLG device under THz radiation.

Firstly, we intent to gauge whether the photomixer related electronics can disturb transport measurements on the sample. For this purpose, we mount the device in

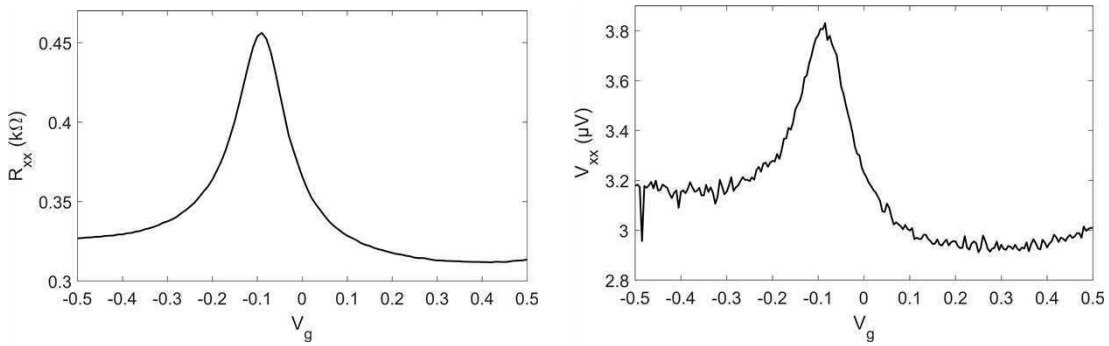

(a) **(b)**

Figure 5.14: SLG 7 gate sweep measurements V_g =-0.5 - 0.5V. a) 4-probe measurement for initial device classification was performed with a current source of $I_B = 10nA$. b) Induced leakage current visible from gatesweep. No external bias applied and the THz path is blocked.

our sample stage and perform a gate-sweep. We enable the photomixer lasers and biasing of ±5 V while blocking the THz radiation with a metal disk in-between emitter and sample. We do not apply any external current to the SLG and measure the potential difference within the hallbar. In an undisturbed sample one would expect a potential that is fully independent from the gate voltage with fluctuations not exceeding the noise floor. Instead we receive a distribution that resembles our previous measurement of the SLG Dirac cone under current bias (Figure 5.14b). Notably, this feature is only present while the photomixer biasing is enabled. We therefore conclude that the external function generator responsible for driving the THz emitter is also indirectly inducing an undesired current within the sample. By using the previously measured resistivity of our device at I_B= 10 mA as a reference, we can calculate the extent of this induced current to ≈ 0.7 nA. This can create significant disturbances, especially in measurements that do not utilise large external currents.

After further analysis we find two pathways for crosstalk causing the undesired emitter-sample interaction. The first is due to the biasing line being located in the same wire bundle as the measurement cables. Even thought the individual lines are reasonably well isolated from one another (20GΩ for DC), the sizable currents ∼mA during photomixer operation still have a significant effect. Especially inductive coupling during the 7.777 7 Hz square wave switching process is of concern to us as these disturbances will be picked up by the Lock-in amplifiers running at the same frequency. Fortunately, our DR possesses a second measurement wire bundle which is fully separated from the other. We therefore only require a second breakout box (Figure 5.15a) and some rewiring to ensure proper isolation.
The second origin of emitter-sample crosstalk interaction is induced by a relative shift in ground levels. Both the cryostat and measurement rack are individually grounded, with no direct connection in-between. The output of the function generator is fed directly into the DR breakout box and they therefore share the same ground via the outer coaxial cable conductor. The Sync cable between function generator and Lock-in amplifiers creates another ground reference. As the Lock-in amplifiers are connected to the rack grounding, it is essential to operate them in floating mode. Otherwise the photomixer bias shifts the relative potential between

the grounds which induces current in the sample.

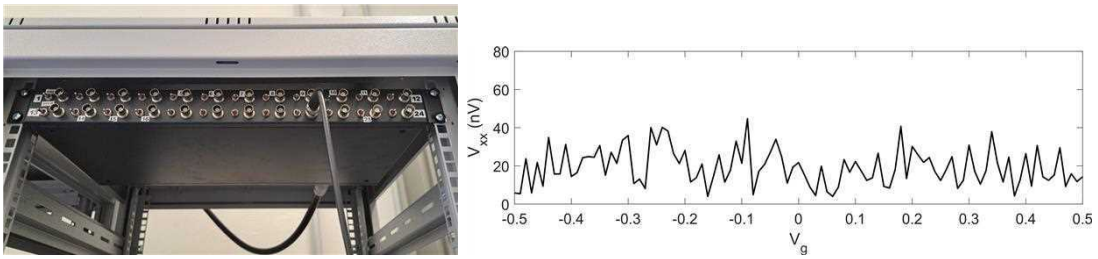

(a) **(b)**

Figure 5.15: Separate breakout box and crosstalk voltage after biasing isolation b) Isolated channel prevents leakage current within sample. b) Resulting voltages traces lack the signature graphene resistivity peak.

After executing these modifications, we no longer receive the previous Dirac cone peak and the crosstalk current is strongly suppressed. The dark voltage (<40 nV) is now (Figure 5.15b) well within the usual noise range ∼nV of such a measurement. We can therefore conclude that our setup is working within expected parameters.

However, even with our setup improvements we do not recover the device responsivity measured by Vicarelli et al. [52]. This is mainly attributed to lower THz intensities, as we currently do not reach full photomixer power with the available maximum bias of 5 V. Due to the quadratic scaling with biasing volateg in (5.5), the maximum possible emission (∼2 µW at 10 V) drops to ∼0.7 µW, with an additional $\sqrt{2}$ factor for polarisation mismatch while the reference experiment was performed at 15 to 1000 µW emission power. Even at full photomixer power our intensity would be significantly lower. It is therefore currently impossible to recover the same response from our SLG device. Additionally, our antenna-sample coupling efficiencies are significantly worse compared to the reference publication. This is because we utilised a different contacting method which leads to higher contact resistance at the interface between gold antenna and graphene. When exchanging the SLG for a much more sensitive MATBG device at cryogenic temperatures, the correlated behaviour of MATBG get involved and we expect to see a variety of novel sample responses.

Chapter 6

Analysis of Superconducting MATBG Devices

Leading up to this thesis, several TBG hallbar devices were manufactured. Due to twist angle inhomogeneity and contamination induced disorder, the local quality of the TBG material can vary strongly, even within the same sample. It is therefore essential to classify each device and its twist-angle via low-temperature transport measurements. As this is not the main focus of this thesis, we will only briefly demonstrate the typical analysis process via a single MATBG device of high quality that exhibits correlated electron states as well as a clear superconducting transition.

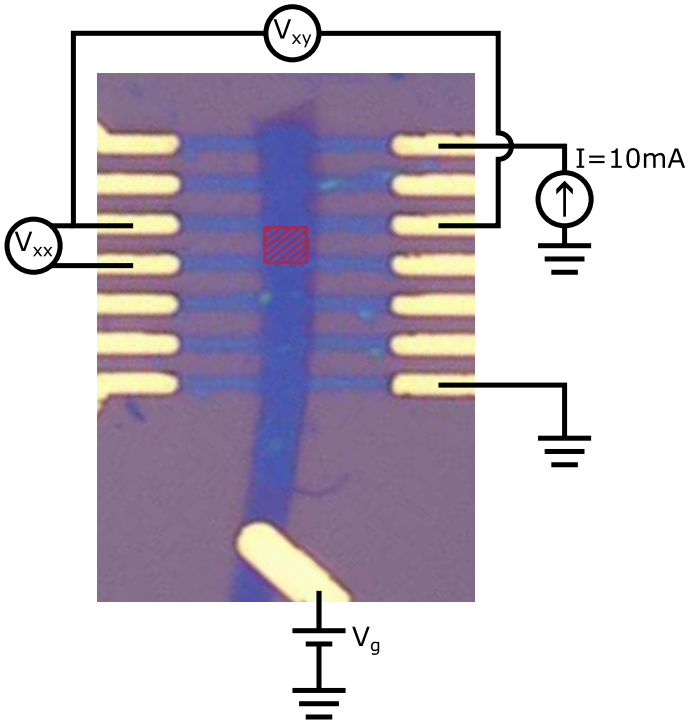

Figure 6.1: Schematic of the 4 Probe Measurement of our MATBG device, studying the logitudinal (V_{xx}) and orthogonal (V_{xy}) potential resulting from an externally induced current within the investigated area (marked in red).

6.1 Twist Angle and Gate Capacitance Extraction

In order to accurately analyse and understand processes within TBG samples, the gate capacitance and especially the twist angle needs to be determined. To achieve this, several methods are well established [15], three of which we will be concentrating on in this thesis.

They are all based on the relation between the super-lattice carrier density n_S, and the twist angle θ (Equ. 2.19). As we can easily determine the location of a filled superlattice band (at V_{BI}=$\pm$1.2 8V in this device) via the maximum resistivity points in the band insulator during gate sweeps (Fig.6.2):

$$n_S = \frac{C_g V_B I}{e} \tag{6.1}$$

We then only require knowledge of the gate capacitance or h-BN dielectric thickness.

6.1.1 Extraction via Integer Quantum Hall Effect

The first method makes use of the Integer Quantum Hall (IQH) effect and the resulting Landau fan pattern of transport measurements under different magnetic fields (Fig. 6.2). The possible electron orbits undergo a transition into discretised orbits. The filling factor of these then contirbutes to the overall conductivity and becomes visible as a Landau fan.

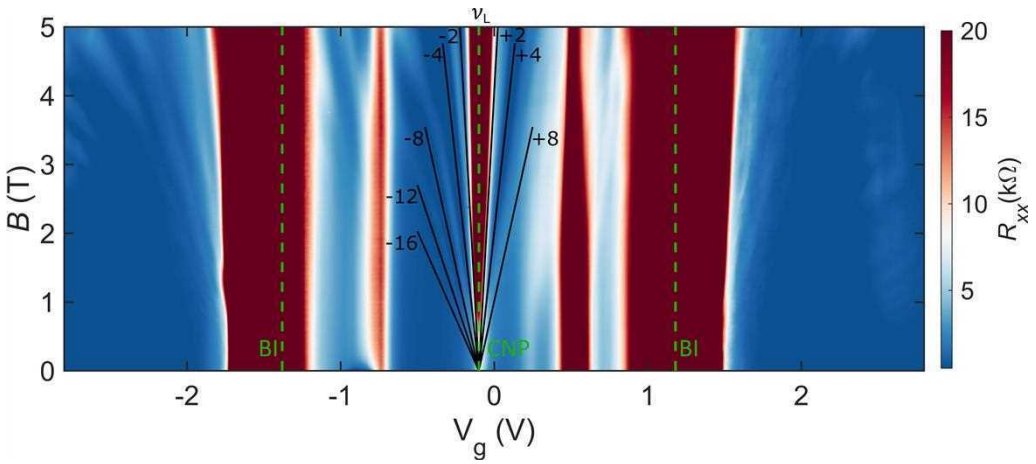

Figure 6.2: Landau fan with Landau levels and their filling-factor in black. Charge neutrality point V_g=-0.1V and the band insulators at V_g=-1.38V and V_g=1.18V indicated in green.

Using the slope dB/dV_g of the Landau levels from Figure 6.2, and the relation:

$$\nu_L = \frac{nh}{eB} = \frac{h}{e^2}\frac{C_g V_g}{B} \tag{6.2}$$

we find a pre-factor of $\nu_L \cdot dB/dV = 81$ T/V, from which we can calculate a capacitance of $C_g = 311$ nF/cm^2 and a twist angle of $\theta = 1.03^\circ$.

6.1.2 Extraction via Hall Conductivity

The second method utilises the classical Hall Conductivity at low magnetic fields, in this case $B = \pm$ 300 mT. We measure the perpendicular Hall resistance R_{xy} where the Hall carrier density n_H can be described via:

$$n_H = -\frac{B}{eR_{xy}} \tag{6.3}$$

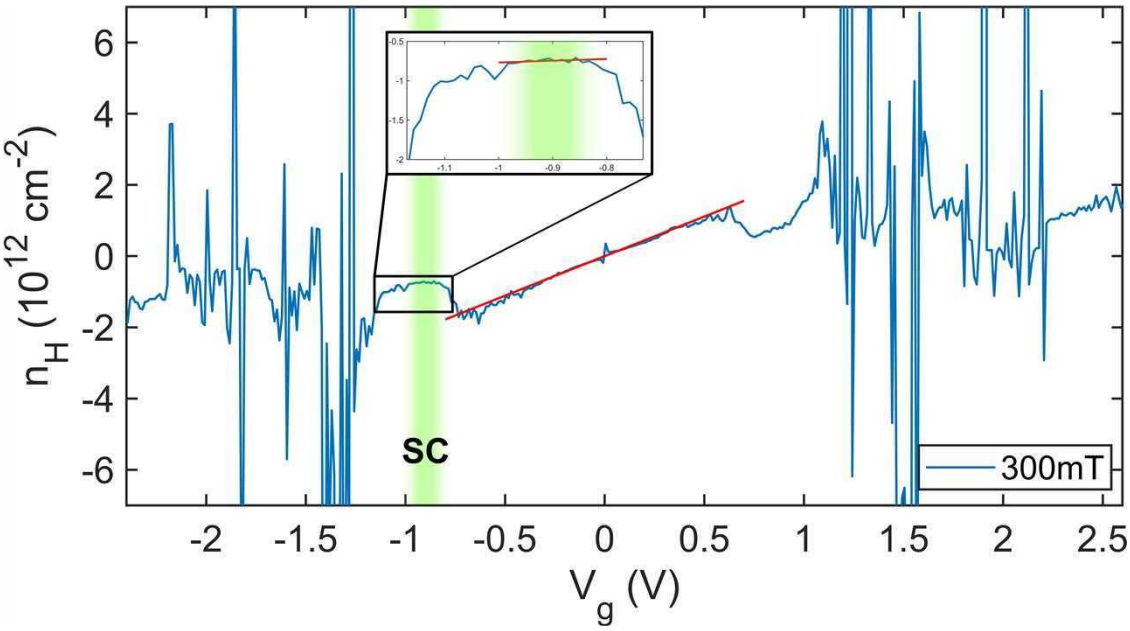

Figure 6.3: Classical hall conductivity Slope of dn_H/dn around the charge neutrality point V_g= 0.1 V and in the superconducting state (enlarged section).

Near the charge neutrality point and at low magnetic fields (classical hall regime), any shift in the gate induced carrier density leads to a proportional offset in the hall carrier density. This is depicted in Figure 6.3 by the linear slope fit which corresponds to $dn_H/dn = 1$ and therefore provides accurate information about the proportionality between V_g and n. This allows us to calculate the superlattice carrier density n_S = -2.84x10^{16}. The resulting capacitance for this device is then C_g = 356 nF/cm^2 with a twist angle of $\theta = 1.11°$.

We can use the same method to also gain information about the free carrier density in the non-classical superconducting state at $V_g = 0.9$V. From the fit in Figure 6.3 we extract a carrier density of $n_H = 2.24 \times 10^{11}$ cm^{-2} in agreement with results from previous publications [17].

6.1.3 Extraction via Gate Dielectric Thickness

Additionally to the transport measurements, we can also determine the h-BN thickness thickness via Atomic Force Microscopy (AFM) right after the stacking process. The different crystal shapes and sizes help us identifying the individual layers (Fig. 6.4).

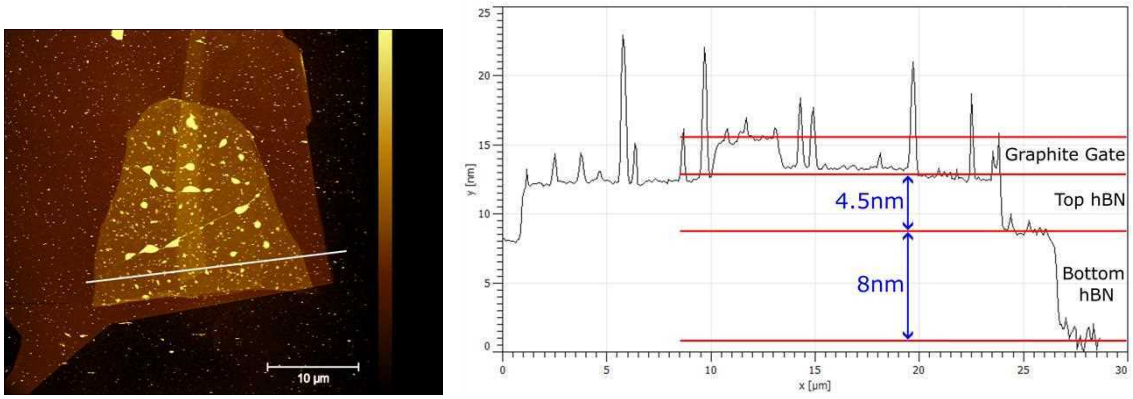

(a) **(b)**

Figure 6.4: AFM and height profile a) AFM image of the raw stack before fabrication, with the location of the height profile indicated in white b) Height profile with corresponding layers

Using the resulting the bottom hBN thickness of $d_{hBN} = 8$nm and the dielectric constant of $\epsilon_{hBN} = 3.4\epsilon_0$ [36] we can estimate the Capacitance and the twist angle to be $C_g = \epsilon/d \approx 376$ nF/cm^2 and $\theta = 1.14°$ respectively.

Summarizing all three methods, the capacitance and twist angle amount to $C_g = 350 \pm 40$ nF/cm^2 and $\theta = 1.09 \pm 0.06°$

6.2 Characterisation of Superconducting State

In order to prove and analyse the superconducting state within our MATBG sample, a number of gate-sweeps at different temperatures and magnetic fields were performed. From this we can clearly demonstrate the presence of superconductivity and extract several essential parameters, namely the critical temperature, critical magnetic field as well as the coherence length. The traces at different temperatures and zero magnetic field in Figure 6.5a show a stark drop in resistivity at a Gate Voltage of $V_g = 0.90$ V below a temperature of $T = 3$ K giving a clear indication of superconductivity.

6.2.1 Critical Temperature

Due to previously discussed inhomogenities in MATBG, the superconducting transition is quite broad and it is impossible to define a specific onset temperature. The critical temperature T_C is therefore defined as the point where the resistivity of our sample drops below 50% of its normal state value. In Figure 6.5b we linearly fit the resistance at $T > 7$ K and from its intersection with the curve we receive a T_C of 1.71 K. The error is defined through the transition temperatures $T_{40} = 1.54$ K and $T_{60} = 1.93$ K at 40% and 60% resistivity respectively. In summary, we arrive at a critical temperature of $T_C = 1.7$ K $\pm$ 0.3 K and matches the theoretical value well.

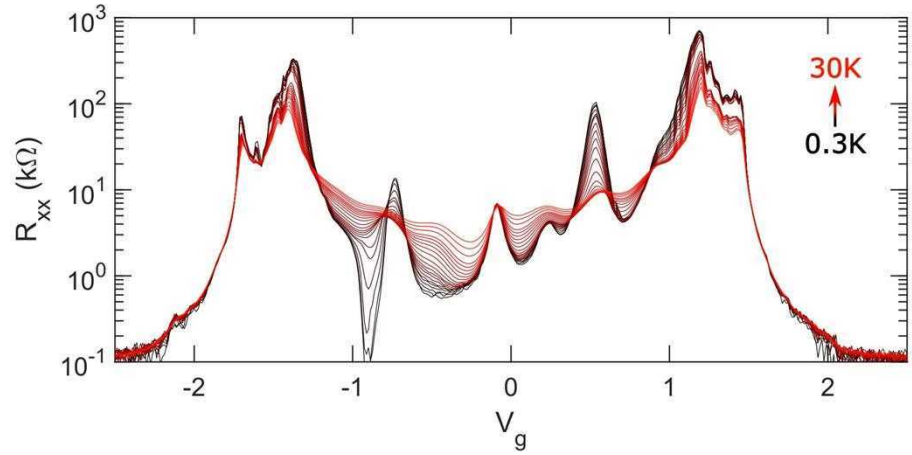

(a)

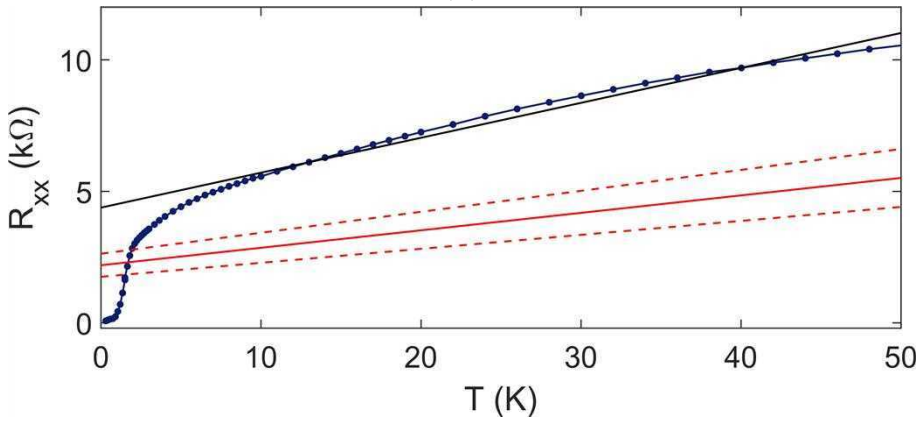

(b)

Figure 6.5: Critical superconducting transition. a) Temperature dependent resistivity versus gate voltage from 0.3 to 30K, with a distinct SC transition at $T < 2$. b) R_{xx} vs T at V_G = -0.90 V, diagonal lines representing the linear fit for the normal state resistivity (black) and its 50% value (red). Dashed lines indicate the error-bar at $\pm 10\%$ resistance

6.2.2 Critical Magnetic Field and Coherence Length

For any superconducting material under a magnetic field, there exists a point at which the cooper pairs split and superconductivity is suppressed. Similarly to the critical temperature, the critical magnetic field B_C is defined at 50% of the normal state resistance. Temperature and magnetic field both contribute to the reduction of electron correlation and therefore higher temperatures lead to lower critical fields. The equation:

$$B_C = \frac{\phi_0}{2\pi\xi_{GL}^2}(1 - \frac{T}{T_C}) \tag{6.4}$$

describes the relation between B_C and T_C, which we can use to calculate the Ginzburg-Landau coherence length ξ_{GL} as well as the London penetration depth

λ_L. They provide a measure for the size of an individual Cooper pair and therefore how deep an external field can penetrate into the SC material. From the data in Figure 6.6b and the resulting fit of equation we receive values for the critical temperature of T_C = 2.1 K± 0.7 K and a coherence length of 55 nm± 7 nm.

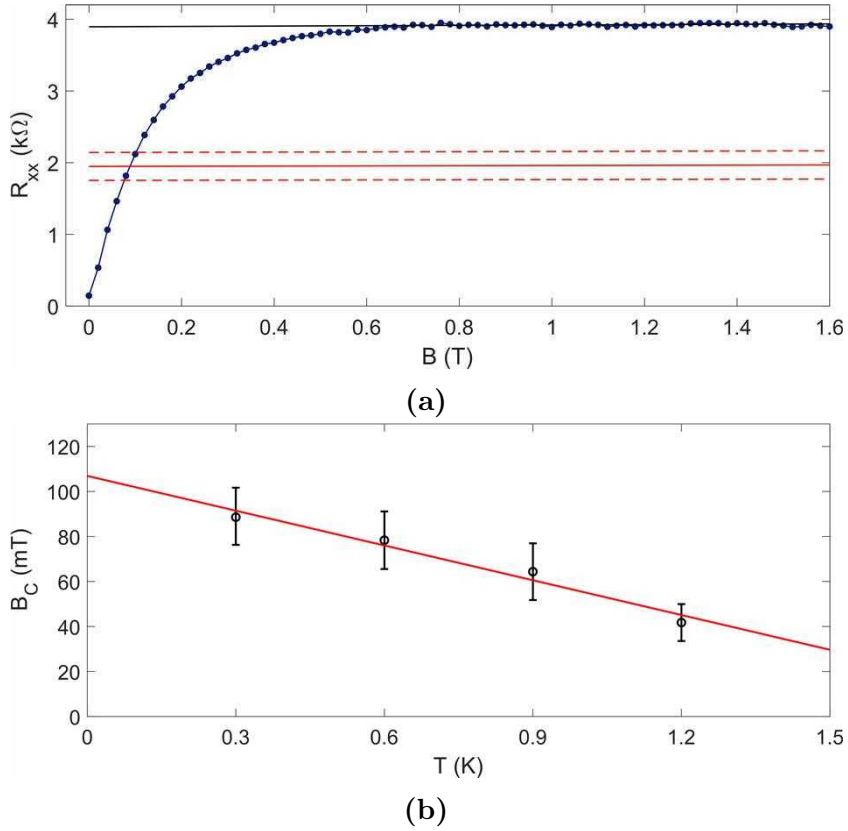

Figure 6.6: Critical Magnetic Field a) Graph of R_{xx} vs B at 300mK and an optimal doping of V_G=-0.9V depicts a well defined SC transition with B_C=89mT. The critical field B_C is extracted from the 50% ± 5% values (red) of non-SC resistance (black linear fit). b) Combined data-points extracted from traces at different temperatures. Fit of equation 6.4 visible in red.

Chapter 7

Conclusion and Outlook

With this thesis we have demonstrated the successful implementation of a cryogenic THz setup. It is now ready for extensive photovoltage experiments in order to investigate the MATBG flattbands as well as detecting THz radiation. Hereby, we bias a MATBG device with a large current. Incident photons then bolometrically break local superconductivity and the resulting non-zero resistance creates further heating which eventually leads to the entire device quenching. This can then be measured as a short ∼ms voltage spike and with a parallel current path the detector can be reset. Single photon sensitivity of such a MATBG device has recently been demonstrated by our group in the near infrared ($\lambda = 1550$ nm) [5]. As long as the photons have enough energy ∼1 eV to break at least least one cooper pair, single photon detection should be theoretically possible within the entire THz spectrum ($f > 300$ GHz). However, achieving this in a real experiment is challenging and will likely require further setup improvements. On the emitter side the upgrades include lenses, wave-plates, higher biasing as well as performing a through beam intensity map. Together with optimizing the antenna shape and its graphene contact we can reach on-sample THz intensities several times larger than in the current configuration. In summary, we have demonstrate our ability to generate well-defined THz emissions which we can used for novel photovoltage experiments on 2D materials.

Bibliography

[1] M. Alattas and U. Schwingenschlögl. "Band Gap Control in Bilayer Graphene by Co-Doping with B-N Pairs". In: *Scientific Reports* 8.1 (Dec. 2018). ISSN: 2045-2322. DOI: 10.1038/s41598-018-35671-2. URL: http://dx.doi.org/10.1038/s41598-018-35671-2.

[2] N. Almtireen, J. J. Brandner, and J. G. Korvink. "Pulse Tube Cryocooler: Phasor Analysis and One-Dimensional Numerical Simulation". en. In: *Journal of Low Temperature Physics* 199.5-6 (June 2020), pp. 1179–1197. ISSN: 0022-2291, 1573-7357. DOI: 10.1007/s10909-020-02378-6. URL: http://link.springer.com/10.1007/s10909-020-02378-6 (visited on 03/27/2024).

[3] *APS Viewpoint*. hhttps://physics.aps.org/articles/v12/104[Accessed: 2024-09-03].

[4] J. Bardeen, L. N. Cooper, and J. R. Schrieffer. "Theory of Superconductivity". In: *Phys. Rev.* 108 (5 Dec. 1957), pp. 1175–1204. DOI: 10.1103/PhysRev.108.1175. URL: https://link.aps.org/doi/10.1103/PhysRev.108.1175.

[5] G. Di Battista et al. *Ultra-low carrier density superconducting bolometers with single photon sensitivity based on magic-angle twisted bilayer graphene*. 2024. arXiv: 2403.02049 [cond-mat.mes-hall]. URL: https://arxiv.org/abs/2403.02049.

[6] B. Andrei Bernevig and Dmitri K. Efetov. "Twisted bilayer graphene's gallery of phases". In: *Physics Today* 77.4 (Apr. 2024), pp. 38–44. ISSN: 1945-0699. DOI: 10.1063/pt.jvsd.yhyd. URL: http://dx.doi.org/10.1063/pt.jvsd.yhyd.

[7] Rafi Bistritzer and Allan H. MacDonald. "Moiré bands in twisted double-layer graphene". In: *Proceedings of the National Academy of Sciences* 108.30 (July 2011), pp. 12233–12237. ISSN: 1091-6490. DOI: 10.1073/pnas.1108174108. URL: http://dx.doi.org/10.1073/pnas.1108174108.

[8] *Bluefors Website*. https://bluefors.com/products/dilution-refrigerator-measurement-systems/sd-dilution-refrigerator-measurement-system/ [Accessed: 2024-08-14].

[9] *Bluefors Website*. [Accessed: 2024-08-14] https://bluefors.com/products/pulse-tube-cryocoolers/.

[10] *Bluefors Website*. [Accessed: 2024-08-25] https://bluefors.com/products/measurement-infrastructure/coaxial-wiring/.

[11] Yuan Cao et al. "Correlated insulator behaviour at half-filling in magic-angle graphene superlattices". In: *Nature* 556.7699 (Mar. 2018), pp. 80–84. ISSN: 1476-4687. DOI: 10.1038/nature26154. URL: http://dx.doi.org/10.1038/nature26154.

[12] Yuan Cao et al. "Unconventional superconductivity in magic-angle graphene superlattices". In: *Nature* 556.7699 (Mar. 2018), pp. 43–50. ISSN: 1476-4687. DOI: 10.1038/nature26160. URL: http://dx.doi.org/10.1038/nature26160.

[13] A. H. Castro Neto et al. "The electronic properties of graphene". In: *Rev. Mod. Phys.* 81 (1 Jan. 2009), pp. 109–162. DOI: 10.1103/RevModPhys.81.109. URL: https://link.aps.org/doi/10.1103/RevModPhys.81.109.

[14] Hong Cui et al. "Spectral characteristic of single layer graphene via terahertz time domain spectroscopy". In: *Optik* 126.14 (July 2015), pp. 1362–1365. ISSN: 0030-4026. DOI: 10.1016/j.ijleo.2015.03.032. URL: http://dx.doi.org/10.1016/j.ijleo.2015.03.032.

[15] Ipsita Das. "Investigation of the Interaction Driven Quantum Phases in Magic-Angle Twisted Bilayer Graphene". PhD thesis. ICFO, LMU, 2023.

[16] Wolfgang Demtröder. *Experimentalphysik 3: Atome, Moleküle und Festkörper; 3rd ed.* Springer-Lehrbuch. Berlin: Springer, 2005.

[17] Giorgio Di Battista et al. "Revealing the Thermal Properties of Superconducting Magic-Angle Twisted Bilayer Graphene". In: *Nano Letters* 22.16 (Aug. 2022), pp. 6465–6470. ISSN: 1530-6992. DOI: 10.1021/acs.nanolett.1c04512. URL: http://dx.doi.org/10.1021/acs.nanolett.1c04512.

[18] J. Diez-Merida et al. *High-yield fabrication of bubble-free magic-angle twisted bilayer graphene devices with high twist-angle homogeneity.* 2024. DOI: 10.48550/ARXIV.2405.11323. URL: https://arxiv.org/abs/2405.11323.

[19] I.S. Gregory et al. "Optimization of photomixers and antennas for continuous-wave terahertz emission". In: *IEEE Journal of Quantum Electronics* 41.5 (May 2005), pp. 717–728. ISSN: 0018-9197. DOI: 10.1109/jqe.2005.844471. URL: http://dx.doi.org/10.1109/JQE.2005.844471.

[20] Asif Hayat et al. "Recent advances, properties, fabrication and opportunities in two-dimensional materials for their potential sustainable applications". In: *Energy Storage Materials* 59 (May 2023), p. 102780. ISSN: 2405-8297. DOI: 10.1016/j.ensm.2023.102780. URL: http://dx.doi.org/10.1016/j.ensm.2023.102780.

[21] *Heidelberg Instruments Website*. https://heidelberg-instruments.com/product/mla/[Accessed: 2024-09-01].

[22] Yuan Huang et al. "Reliable exfoliation of large-area high-quality flakes of graphene and other two-dimensional materials". In: *ACS nano* 9.11 (2015), pp. 10612–10620.

[23] Carl A. Hudeczek. "Finite Element Analysis and Fabrication of a Bow-tie Antenna for Terahertz Detection". Bachelor's Thesis. 2024.

[24] Md. Saiful Islam et al. "Terahertz optical fibers [Invited]". In: *Optics Express* 28.11 (May 2020), p. 16089. ISSN: 1094-4087. DOI: 10.1364/oe.389999. URL: http://dx.doi.org/10.1364/OE.389999.

[25] Sandeep Joy, Saad Khalid, and Brian Skinner. *Transparent mirror effect in twist-angle-disordered bilayer graphene*. Aug. 2020.

[26] Young-Chan Kim et al. "High-Speed High-Resolution Terahertz Time-Domain Spectrometer". In: *Korean Journal of Optics and Photonics* 19 (Oct. 2008), pp. 370–375. DOI: 10.3807/HKH.2008.19.5.370.

[27] Charles Kittel. *Introduction to Solid State Physics*. John Wiley & Sons, Inc., 2005.

[28] Marion Lang, Anselm Deninger, and AG Toptica Photonics. "Laser-based terahertz generation & applications". In: *Photonik international* 4 (2012), pp. 36–38.

[29] J. M. B. Lopes dos Santos, N. M. R. Peres, and A. H. Castro Neto. "Continuum model of the twisted graphene bilayer". In: *Phys. Rev. B* 86 (15 Oct. 2012), p. 155449. DOI: 10.1103/PhysRevB.86.155449. URL: https://link.aps.org/doi/10.1103/PhysRevB.86.155449.

[30] J. M. B. Lopes dos Santos, N. M. R. Peres, and A. H. Castro Neto. "Graphene Bilayer with a Twist: Electronic Structure". In: *Physical Review Letters* 99.25 (Dec. 2007). ISSN: 1079-7114. DOI: 10.1103/physrevlett.99.256802. URL: http://dx.doi.org/10.1103/PhysRevLett.99.256802.

[31] Siyuan Luo et al. "Graphene-based optical modulators". In: *Nanoscale Research Letters* 10.1 (Apr. 2015). ISSN: 1556-276X. DOI: 10.1186/s11671-015-0866-7. URL: http://dx.doi.org/10.1186/s11671-015-0866-7.

[32] M L Meade. "Advances in lock-in amplifiers". In: *Journal of Physics E: Scientific Instruments* 15.4 (Apr. 1982), pp. 395–403. ISSN: 0022-3735. DOI: 10.1088/0022-3735/15/4/001. URL: http://dx.doi.org/10.1088/0022-3735/15/4/001.

[33] Jaime Díez Mérida. "Probing Magic-Angle Twisted Bilayer Graphene with Monolithic Gate-Defined Josephson Junctions". PhD thesis. ICFO, UPC, 2024.

[34] Pilkyung Moon and Mikito Koshino. "Energy spectrum and quantum Hall effect in twisted bilayer graphene". In: *Phys. Rev. B* 85 (19 May 2012), p. 195458. DOI: 10.1103/PhysRevB.85.195458. URL: https://link.aps.org/doi/10.1103/PhysRevB.85.195458.

[35] K. S. Novoselov et al. "Electric Field Effect in Atomically Thin Carbon Films". In: *Science* 306.5696 (Oct. 2004), pp. 666–669. ISSN: 1095-9203. DOI: 10.1126/science.1102896. URL: http://dx.doi.org/10.1126/science.1102896.

[36] A Pierret et al. "Dielectric permittivity, conductivity and breakdown field of hexagonal boron nitride". In: *Materials Research Express* 9.6 (June 2022), p. 065901. ISSN: 2053-1591. DOI: 10.1088/2053-1591/ac4fe1. URL: http://dx.doi.org/10.1088/2053-1591/ac4fe1.

[37] Frank Pobell. *Matter and Methods at Low Temperatures*. Springer, 2007.

[38] Sascha Preu et al. *Principles of THz Generation*. July 2015. DOI: 10.1002/9781118920411.ch2. URL: http://dx.doi.org/10.1002/9781118920411.ch2.

[39] A.V. Rozhkov et al. "Electronic properties of graphene-based bilayer systems". In: *Physics Reports* 648 (Aug. 2016), pp. 1–104. ISSN: 0370-1573. DOI: 10.1016/j.physrep.2016.07.003. URL: http://dx.doi.org/10.1016/j.physrep.2016.07.003.

[40] Michael G. Scheer, Kaiyuan Gu, and Biao Lian. "Magic angles in twisted bilayer graphene near commensuration: Towards a hypermagic regime". In: *Physical Review B* 106.11 (Sept. 2022). ISSN: 2469-9969. DOI: 10.1103/physrevb.106.115418. URL: http://dx.doi.org/10.1103/PhysRevB.106.115418.

[41] Paul Seifert et al. "Magic-Angle Bilayer Graphene Nanocalorimeters: Toward Broadband, Energy-Resolving Single Photon Detection". In: *Nano Letters* 20.5 (Apr. 2020), pp. 3459–3464. ISSN: 1530-6992. DOI: 10.1021/acs.nanolett.0c00373. URL: http://dx.doi.org/10.1021/acs.nanolett.0c00373.

[42] Nabila Shamim et al. "Glass transition temperature of thin polycarbonate films measured by flash differential scanning calorimetry". en. In: *Journal of Polymer Science Part B: Polymer Physics* 52.22 (Nov. 2014), pp. 1462–1468. ISSN: 08876266. DOI: 10.1002/polb.23583. URL: https://onlinelibrary.wiley.com/doi/10.1002/polb.23583 (visited on 04/02/2024).

[43] F. Sizov and A. Rogalski. "THz detectors". In: *Progress in Quantum Electronics* 34.5 (Sept. 2010), pp. 278–347. ISSN: 0079-6727. DOI: 10.1016/j.pquantelec.2010.06.002. URL: http://dx.doi.org/10.1016/j.pquantelec.2010.06.002.

[44] T.W.G. Solomons and C. Fryhle. *Organic Chemistry*. John Wiley & Sons, 2009. ISBN: 9780470401415. URL: https://books.google.de/books?id=E4VylgguUR8C.

[45] G. R. Stewart. "Unconventional superconductivity". In: *Advances in Physics* 66.2 (Apr. 2017), pp. 75–196. ISSN: 1460-6976. DOI: 10.1080/00018732.2017.1331615. URL: http://dx.doi.org/10.1080/00018732.2017.1331615.

[46] *Thorlabs Website*. https://www.thorlabs.com/newgrouppage9.cfm?objectgroup_id=949[Accessed: 2024-08-24].

[47] G. Thummes, S. Bender, and C. Heiden. "Approaching the 4He lambda line with a liquid nitrogen precooled two-stage pulse tube refrigerator". In: *Cryogenics* 36.9 (Sept. 1996), pp. 709–711. ISSN: 0011-2275. DOI: 10.1016/0011-2275(96)00060-4. URL: http://dx.doi.org/10.1016/0011-2275(96)00060-4.

[48] Nikhil Tilak et al. "Flat band carrier confinement in magic-angle twisted bilayer graphene". In: *Nature Communications* 12.1 (July 2021). ISSN: 2041-1723. DOI: 10.1038/s41467-021-24480-3. URL: http://dx.doi.org/10.1038/s41467-021-24480-3.

[49] *Toptica Photonics AG*. https://www.toptica.com/products/terahertz-systems/frequency-domain/gaas-and-ingaas-photomixers[Accessed: 2024-08-29].

[50] *Toptica Photonics AG*. https://www.toptica.com/technology/technical-tutorials/terahertz/cw-terahertz[Accessed: 2024-08-24].

[51] J J Valois, G F Nellis, and J M Pfotenhauer. "Characterization of the thermal properties of OFHC copper at cryogenic temperature". In: *IOP Conference Series: Materials Science and Engineering* 1301.1 (May 2024), p. 012167. ISSN: 1757-899X. DOI: 10.1088/1757-899x/1301/1/012167. URL: http://dx.doi.org/10.1088/1757-899X/1301/1/012167.

[52] L. Vicarelli et al. "Graphene field-effect transistors as room-temperature terahertz detectors". In: *Nature Materials* 11.10 (Sept. 2012), pp. 865–871. ISSN: 1476-4660. DOI: 10.1038/nmat3417. URL: http://dx.doi.org/10.1038/NMAT3417.

[53] Gwyn P Williams. "Filling the THz gap—high power sources and applications". In: *Reports on Progress in Physics* 69.2 (Dec. 2005), pp. 301–326. ISSN: 1361-6633. DOI: 10.1088/0034-4885/69/2/r01. URL: http://dx.doi.org/10.1088/0034-4885/69/2/R01.

[54] H. Zu, W. Dai, and A.T.A.M. de Waele. "Development of dilution refrigerators—A review". In: *Cryogenics* 121 (Jan. 2022), p. 103390. ISSN: 0011-2275. DOI: 10.1016/j.cryogenics.2021.103390. URL: http://dx.doi.org/10.1016/j.cryogenics.2021.103390.

I hereby declare that this thesis is my own work, and that I have not used any sources and aids other than those stated in the thesis.

München, date of submission
Leon Schubert